Doctoral Dissertations and Master's Theses

Fall 12-2015

Computation of Hypersonic Flows with Lateral Jets Using k-ω Turbulence Model

Spatika Dasharati Iyengar
Embry-Riddle Aeronautical University

Follow this and additional works at: https://commons.erau.edu/edt

Part of the Astrodynamics Commons

COMPUTATION OF HYPERSONIC FLOWS WITH LATERAL

JETS USING k-ω TURBULENCE MODEL

A Thesis

Submitted to the Faculty

of

Embry-Riddle Aeronautical University

by

Spatika Dasharati Iyengar

In Partial Fulfillment of the

Requirements for the Degree

of

Master of Science in Aerospace Engineering

December 2015

Embry-Riddle Aeronautical University

Daytona Beach, Florida

COMPUTATION OF HYPERSONIC FLOWS WITH LATERAL JETS USING k-ω TURBULENCE MODEL
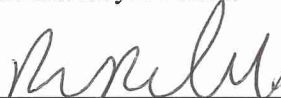
by

Spatika Dasharati Iyengar

A Thesis prepared under the direction of the candidate's committee chairman, Dr. Eric Perrell, Department of Aerospace Engineering, and has been approved by the members of the thesis committee. It was submitted to the School of Graduate Studies and Research and was accepted in partial fulfillment of the requirements for the degree of Master of Science in Aerospace Engineering
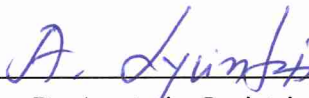
THESIS COMMITTEE

_____
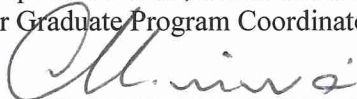Chairman, Dr. Eric Royce Perrell

_____
Member, Dr. Reda Mankbadi

_____
Member, Dr. Anastasios Lyrintzis

_____
Department Chair, Dr. Anastasios Lyrintzis
or Graduate Program Coordinator, Dr. Eric Perrell

20 Nov 15
Date

_____
Dean of College of Engineering, Dr. Maj Mirmirani

12/2/15
Date

_____
Associate Chancellor for academics, Dr. Christopher Grant

12/4/15
Date

ACKNOWLEDGMENTS

Foremost, I would like to express my deepest gratitude to my Thesis Advisor, Dr. Eric Royce Perrell, for his continuous support, patience, motivation, enthusiasm, and immense knowledge. Besides my advisor, I would like to thank the rest of my thesis committee: Dr. Reda Mankbadi, and Dr. Anastasios Lyrintzis, for their encouragements and insightful comments.

Last but not the least, I would like to thank my family for supporting me throughout my life.

TABLE OF CONTENTS

LIST OF TABLES

LIST OF FIGURES

SYMBOLS

L	Length of the cylindrical body
D_{outer}	Outer diameter of the cylindrical body
D_{inner}	Inner diameter of the cylindrical body
l	Length of the spike
Φ_{outer}	Outer Diameter of spike
Φ_{inner}	Inner Diameter of spike
C_P	Specific heat at constant pressure
C_{lim}	Stress limiter strength
E	Specific total energy
f_β	Vortex-stretching function
F_I, G_I, H_I	Inviscid flux vectors in x,y,z direction
F_V, G_V, H_V	Viscous flux vectors in x,y,z direction
F_I', G_I', H_I'	Inviscid flux vectors in ξ, η, ζ direction
F_V', G_V', H_V'	Viscous flux vectors in ξ, η, ζ direction
F^+, F^-	Positive and negative flux vector
k	Turbulence Kinetic Energy
L	Left eigen vectors for conservative flux Jacobian
P	Mean static pressure
p_fs	Freestream pressure
Pr	Prandtl number
$q_L, \ q_T$	Laminar, Turbulent Heat flux vector
Re_x	Reynolds number at station x
S	Source term vector
S_{ij}	Mean strain-rate tensor
$\overline{S_{ij}}$	Mean strain-rate tensor in computational domain
t	time
$\bar{T}$	Favre-averaged Temperature
T_fs	Free-stream temperature
u,v,w	Components of free stream velocity

u_fs, v_fs, w_fs	Components of freestream velocity
$u_i, \bar{u_i}$	Instantaneous, mean velocity
u_i''	Fluctuating component of velocity
$\bar{u}, \bar{v}, \bar{w}$	Favre-averaged velocity components in x, y, z directions
$\bar{u}', \bar{v}', \bar{w}'$	Favre-averaged velocity components in ξ, η, ζ directions
V	Non-conservative state vector
x, y, z	Rectangular Cartesian coordinates(physical space)
γ	Specific Heat Ratio
δ_{ij}	Kronecker Delta
κ	Thermal conductivity
λ	Eigen values of flux Jacobian
μ	Dynamic viscosity
μ_T	Eddy viscosity
ξ, η, ζ	Curvilinear coordinates(computational plane)
ξ_x	Metrics
$\bar{\rho}$	Mean density
$\bar{\tau}_{Lij}, \bar{\tau}_{Tij}$	Laminar, Reynolds stress tensors (using Favre-averaged velocities)
χ_ω	Dimensionless vortex-stretching parameter
ω	Specific Dissipation rate
Ω_{ij}	Mean-rotation sensor
ε	Correction factor for near sonic velocities in Steger-Warming
β*	Closure coefficient
δ	Boundary layer thickness
u_τ	Friction velocity
y+	Dimensionless wall spacing
D_{fluid}	Drag on the fluid
D_{body}	Drag on the body
A_{in}	Area at the inlet of the control volume
A_{out}	Area at the outlet of the control volume

ABBREVIATIONS

TPS	Thermal Protection system
NaTPS	Non-Ablative Thermal Protection system
CAAA	China Academy of Aerospace and Aerodynamics
TSP	Temperature Sensitive Paint Method
RANS	Reynolds Averaged Navier-Stokes

ABSTRACT

Iyengar, Spatika Dasharati MSAE, Embry-Riddle Aeronautical University, December 2015. Computation of Hypersonic flows with Lateral Jets using k-ω Turbulence Model.

Thermal Protection systems(TPS) are used as shields in space vehicles which encounter high heat and temperatures at the reentry altitudes. Among them, the cooling techniques and the ablative coatings are most popular. However, they have their own weight limitations. In the recent decade, another classification of TPS called the Non-Ablative Thermal Protection systems (NaTPS) have gained significance. The spike-lateral jet method is an NaTPS concept proposed for drag and heat flux reduction in hypersonic nose cones. Numerical simulations are conducted to analyze the effectiveness of spike-lateral jet concept at re-entry altitudes. The spike attached to the hemispherical nose has two circular orifices which eject air. The freestream conditions include Mach number 6 and standard atmospheric conditions at 30 km altitude. The k-ω turbulent model is used to model the case. It is apparent from the results that the lateral jet reconstructs the flow field by pushing the conical shock away and creating a large recirculation zone in front of the blunt body. This pushes the reattachment region rearward thus decreasing peak pressure and heat transfer to the body. The peak pressure at the flow reattachment point on the blunt body can be reduced by 35.9% for the laminar case and 30.3% for the turbulent case. The heat flux can be reduced by 54.1% for laminar case and 64.3% for the turbulent case. Lateral jet injection did not reduce drag as proposed, instead it increases drag by 65.7% and 59.1% for laminar and turbulent cases respectively. Base drag is not included in drag calculations. Results show that it might be promising for future applications of heat flux reduction and peak pressure reduction in reentry vehicles.

1. Introduction

One of the major problems in aerospace engineering is the prediction of hypersonic flows around space vehicles during reentry. Some of the difficulties include: complex physical and chemical phenomena that demand intricate numerical models, high temperatures and velocities in combination with low densities which hinder flow reproduction in ground-based experiments, and aerodynamic heating at reentry conditions. Aerodynamic heating is a significant challenge for reentry vehicles. When the flow is slowed down, the kinetic energy in the flow is converted to heat causing a rise in temperature. This heat is then conducted to the surface materials from the high temperature air. This results in an increase in temperature of the material and loss of energy from the flow. The forced convection replenishes the gases to continue the process.

The nosecones cannot sustain such high temperatures; hence, alternative methods have to be employed to prevent them from burning out. The different methods may include use of ablative heat shields, heat sink metal alloys, high temperature insulations, cooling techniques like radiative cooling, insulation cooling, convective cooling, and transpiration cooling. However, the amount of high temperature material required is significant and will impose a severe penalty on the vehicle's performance. Hence, new concepts of Non-Ablative Thermal Protection system (NaTPS) like spike-blunt body structure, forward-facing jet injection, spike-lateral jet combination and focused energy depositions have been proposed to overcome the disadvantages of ablative systems.

1.1 NaTPS Concepts:

The NaTPS can be classified into two types: shock-wave reconstruction methods and energy deposition techniques. A brief description of various NaTPS concepts are given in the journal article by Liu and Jiang(2013). According to that, in the shock-wave reconstruction methods, the position of shock waves and their interaction points are altered along with modification in aerodynamic configuration. In energy deposition techniques, the flow field is modified by focused energy depositions like pulsed laser

focusing, plasma arcs, electron beams, microwaves, pulsed detonations etc. However, the energy deposition techniques are practically impossible due to large power budget and system complexity (Liu and Jiang, 2013).

1.2   Shock wave reconstruction methods:

One of the more effective concepts proposed is the installation of a physical spike in front of the blunt body. Numerical investigations related to spike-blunt body structure started around 1980's. It was done by various researchers like J.M Shoemaker, Fujita M, Kubota H, R.C. Mehta, Kamran N and his team, as mentioned in article by Gauer & Paull(2008). The spike reconstructs the bow shock into a conical shock and drastically changes the flow field pattern. It creates a recirculation area in front of the blunt nose cone, a flow separation shock that separates the inviscid flow from the recirculation region and a reattachment shock that emerges from the blunt nosecone. The dynamic pressure in the recirculation region is reduced resulting in less heat load on the surface. Nevertheless, the spike-blunt body structure becomes ineffective with a non-zero angle of attack. To overcome the above problem, an aerodisk structure may be used. An aerodisk is a modified aerospike which has a disk attached to the nose of the spike. In both cases, the shock- shock interaction that occurs at the reattachment point on the blunt body results in extremely high pressure at the interaction point. Moreover, severe aerodynamic heating at the spike tip and at the shock reattachment point on the blunt body precludes its application to hypersonic flows (Gauer & Paull, 2008; Mehta, 2000; Liu & Jiang, 2013)
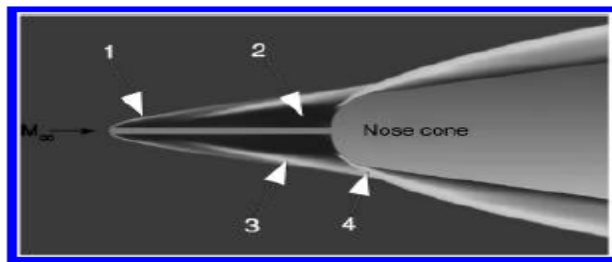
Figure 1.1. Aerospike-induced flow-field: 1) spike bow shock, 2) recirculation area, 3) flow separation shock, and 4) reattachment shock (Gauer & Paull, 2008).

Structural spikes have been successfully tested on launch vehicles and missiles. The spike has low drag during launch and provides high volumetric efficiency by using a blunt cone instead of a slender body. However, at high velocities, the spike suffers from excess heat and ablation due to high stagnation temperatures and structural loadings. The nose cone is a disposable element in the launch vehicle but for a cruise vehicle it would be a permanent element. Damage to a spike due to heating would be intolerable. Hence innovative alternatives were devised to reduce stagnation heat flux for a spike (Marley and Riggins, 2011).

The forward-facing jet was suggested to replace the physical spike around 1960's. A detailed explanation of the investigation can be found in Remeo & Sterrett(1963). The jet reduced the heat flux at the stagnation point and created recirculation which cooled the nosecone. Pressurized gases like air, nitrogen, helium, hydrogen, liquids or solid powders could be used, but, the pressure of the gas had to be higher than the local stagnation pressure to achieve desired results. Another drawback was the drag reduction depended on the flight angle of attack. Even a 2 degree angle of attack would reduce the efficiency of the jet. With the demand for higher requirements of Thermal Protection Systems (TPS) and limitations in flight range, the idea of forward-facing jets has fallen out of favor (Remeo & Sterrett, 1963; Meyer, Nelson and Riggins, 2001; Marley and Riggins, 2011; Liu & Jiang, 2013).

The concept to be investigated here includes a combination of both the above structures. It was tested both numerically and experimentally by Liu and Jiang(2013). A spike-blunt body structure was united with lateral jet injection for obtaining an efficient shock reconstruction. The spike recasts the bow shock as a conical shock and the lateral jets push the shock away from the blunt body and also cool the spike tip. Thus shock-shock interaction is minimized to reduce drag and aerodynamic heating of the nosecone. Another advantage of lateral jets is that the ejection pressure is less than that needed for forward-facing jet. The lateral jet could be gases stored or evaporated coolants that are used in vehicles (Liu and Jiang, 2013).
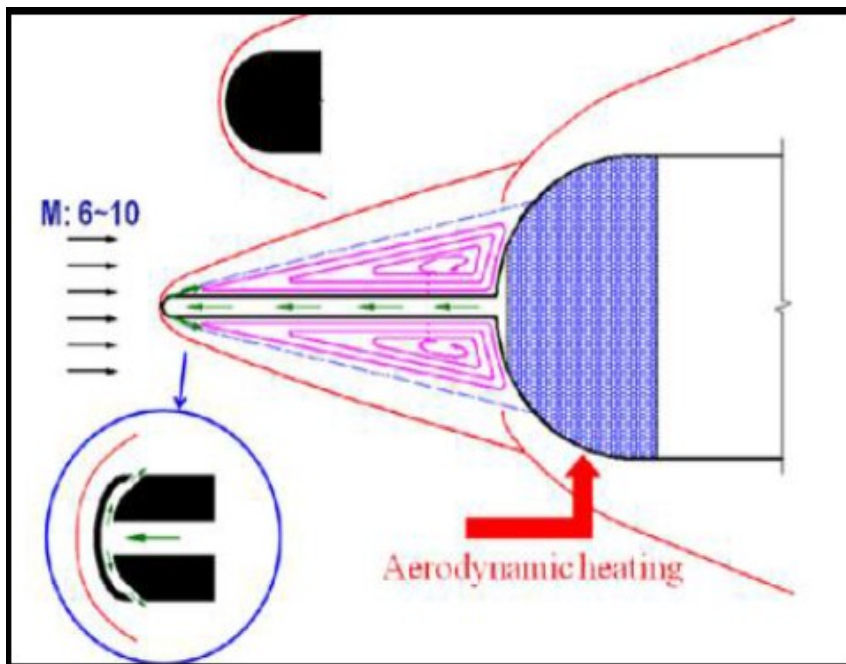
Figure 1.2. Working principle of spike-lateral jet combination (Liu and Jiang, 2013).

1.3   Previous Work

In the previous decades, extensive numerical studies have been carried out to substantiate various NaTPS concepts. Nevertheless, very little experimentation has been conducted to corroborate them, because replicating every aspect of physical and chemical non-equilibrium at hyper-velocities is not practical.

1.3.1   Experimental Work

The first studies conducted utilized different shapes and lengths of spikes as potential candidates for drag reduction and thermal protection.

Research was conducted at University of Tokyo to examine the effect of spike length, shape, spike nose configuration and angle of attack on reduction of heat flux. The details of the research can be found in the article published by Motoyama, Mihara, Miyajima, Watanuki and Kubota, (2001).The experiments were conducted in a Mach 7 Hypersonic Wind Tunnel. The stagnation temperature was 860K and the freestream Reynolds number was 4.0×10^{5}. The aerospike model was a simple stick configuration and the aerodisk

consisted of a disk at its nose. These spikes were threaded at the base and screwed into the hemispherical ceramic body. Temperature Sensitive Paint(TSP) method was chosen for measuring the temperature of the body surface. The fluorescence coating on the body gained energy by UV lamp with appropriate wavelength, and it would undergo a transition from its ground state to an excited state. The resultant output is picked up by a camera to measure the emission intensity of molecules. A calibration that relates emission intensity to the temperature of the coatings was then used to measure temperature. The heat transfer rate was then calculated from the temperature readings using a data reduction model that was based on the solution of one dimensional unsteady heat conduction equation.

The results obtained for the aerospike case show that, both for a conical and a hemispherical spike, a shear layer occurs and at the reattachment point, a high temperature region can be observed. In the aerodisk case, the bow shock is generated far behind on the shoulder of the hemispherical body. The body is completely engulfed within the large recirculation region, which is separated from the inviscid flow within the bow shock by a flow separation shock. Thus, there is no region where the temperature rises significantly. Each spike is effective in reducing the heat flux in the stagnation region. However, at the shoulder of the hemispherical body, where the reattachment of the shear layer in the aerospike case and the impingement of the oblique shock in the aerodisk case happens, the heat flux is higher than the no-spike case. The points of separation and reattachment of the shear layers can be identified by calculating the heat fluxes. The shear layer is a region of low pressure and temperature, and the gradients at the reattachment points produce larger heat fluxes and peak pressures. The pressure drag was calculated assuming Newtonian flow. A sharp pressure peak occurs on the shoulder of the blunt body in the aerospike case, while there is no evident pressure peak on the blunt body for the aerodisk case. The spike is effective even at angles of attack about 8 degrees but the large pitching moment produced by the spike itself should be compensated. Research concluded that the reduction of aerodynamic heating and drag was more successful with use of an aerodisk (Marley and Riggins, 2011; Motoyama, Mihara, Miyajima, Watanuki and Kubota, 2001).

(a) Conical aerospike   (b) Hemispherical aerospike

(c) Hemispherical aerodisk   (d) Flat-faced aerodisk
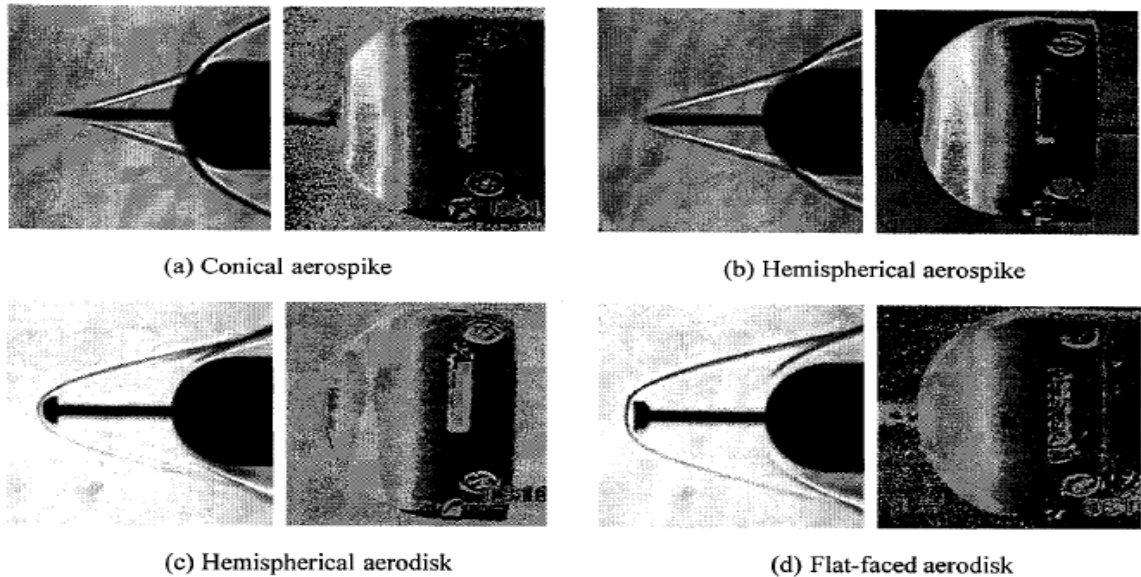
Figure 1.3. Schlieren photographs and surface temperature distribution (Motoyama, 2001)

Similar studies were conducted by Menezes(2003) at HST2 Hypersonic Shock Tunnel at Indian Institute of Science. The shock structures around the spiked blunt nose cones were visualized using an electric discharge technique. The various configurations tested were: a flat disk-tipped spike, a hemispherical disk-tipped spike, a flat tipped spike, and a sharp tipped spike. A 70 mm base diameter blunt cone model fabricated using Bakelite hylem was fitted with a 12mm long, 2mm diameter spike. An electric discharge of about 2 μs was created after obtaining steady flow conditions in the tunnel. The experimental results highlight that for disk-tipped spikes, the heat transfer rates were substantially low (approximately $10W/cm^2$), as the separation bubble completely engulfs the blunt body. The results also showed higher heat flux rates for the flat tipped spike and the sharp tipped spike as the shear layer is limited. Fluctuations measured in the heat transfer rates indicated the oscillatory behavior of the separation bubble. With an increase in angle of attack, the heat transfer rates were increased due to the inward shift of the reattachment points in all types of spike configurations. At low angles of attack about 5 degrees, 40-55% of drag reduction can be achieved using flat and hemispherical aerodisks. The aerospike configuration produces around 20% drag reduction at zero degree angle of attack, but it becomes ineffective at higher angles of attack.
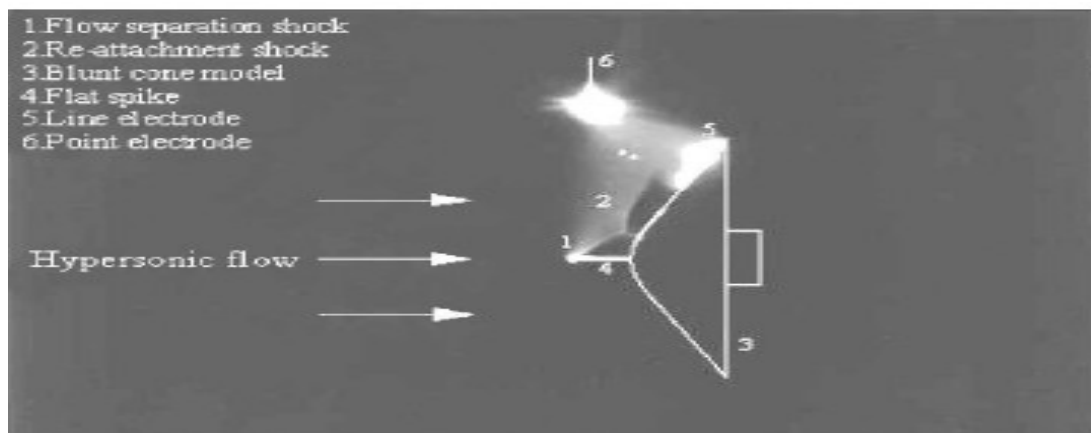
Figure 1.4. Flow field around spiked blunt cone using electric discharge technique (Menezes, 2003)

For a specified spike length, if the flow outside the shear layer can be turned through a smaller angle, an attached conical shock is sufficient to obtain equilibrium between the inviscid stream and the recirculating flow. If the flow has to be turned through a larger angle, a detached shock wave is generated that pushes the high pressure flow into the recirculating region. As the shear layer expands, it pushes the shock upstream thus creating self-excited shock oscillations and flow unsteadiness. Measured surface heat transfer rates with varying spike length indicated that a reduction in the magnitude of flow unsteadiness within the separation bubble near the nose cone can be achieved by varying the spike lengths (Menezes, S. Saravanan, G. Jagadeesh, and K. P. J. Reddy, 2003).

To duplicate the advantages of aerodisks on spikes, lateral jets were used. Flow visualizations were conducted in the hypersonic wind tunnel of FD-07 in China Academy of Aerospace and Aerodynamics (CAAA), Beijing by Liu and Jiang(2013). The wind tunnel has a nozzle of exit diameter 500mm. It was calibrated for Mach number 5.9332. The total pressure in the wind tunnel stagnation section is 20 atm, which is equal to the total pressure at 30km altitude and Mach number 6. The total temperature is 465 K. The static pressure in the flowfield was 1357 Pa. The lateral jet used is air with a total pressure of 5 atm, total temperature 298K and Mach number 2.2. Results indicate that the half angle of the shock is increased up to 60 degrees at the injection position and then

decreases finally to about 30 degrees downstream near the shoulder of the blunt body. The shock wave is pushed away by the lateral jet, thus, the shock-shock interaction point on the shoulder of the blunt body moves further away from the surface. The peak pressure at the reattachment region can be decreased up to 56% for zero degree angle of attack and up to 65% at 4 degree angle of attack thus producing a drag reduction of 50% and 33% respectively. Hence, the lateral jet in conjunction with the aerospike works well in reducing heat flux and drag on blunt bodies (Liu and Jiang, 2013).

Figure 1.5. Test model installed in hypersonic wind tunnel in CAAA (Liu and Jiang, 2013).

1.3.2   Numerical studies

Numerical investigation of spike-blunt body flow started in the late1980's. Many codes were used to solve the compressible viscous Navier-Stokes equations.

In the study by Gauer and Paull (2008), numerical simulations of a spiked blunt body were conducted at different Mach numbers and different altitudes. The drag and heat load reduction were numerically evaluated at Mach numbers 5, 7, and 10. The effect of length of spike on the flowfield was also studied. A blunt spike and an aerodome configuration were studied. An aerodome configuration is a type of aerospike in which the front cone from the sharp spike is replaced with a simple dome to reduce heat loads at the tip of the spike. The flow solver used was CFD-FASTRAN. The solver uses a time marching technique to calculate the flow. The dissociation of species was taken into account.

The flow field calculations were repeated for catalytic wall to consider the effect of recombination and dissociation of species on the wall. The results indicate that for every shape investigated, the heat flux reduction decreases with an increase in Mach number.

However, at Mach numbers closer to 5, there is a remarkable heat load reduction of over 20% for an aerodome configuration when compared to a blunt spike. A fully catalytic wall where all atoms are assumed to recombine yields a 6.5% to 9% increase of heat transfer both in the stagnation region and the nose cone compared to non-reacting cases. A sharp spike results in a 73% increase in stagnation point heat flux when compared to a blunt spike. The sharp spike shows a drag reduction of 35% for the largest spike length (L/D=4 i.e. ratio of length of the spike to the diameter of blunt body).

A drag reduction of 62% can be achieved using an aerodome structure if the L/D ratio remains closer to unity. If L/D ratio for the case increases beyond 2, no significant drag reduction can be achieved.
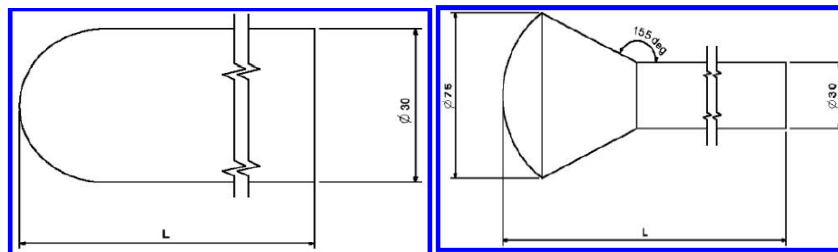
Figure 1.6. Blunt spike(left) and aerodome configuration(right) Gauer and Paull(2008)

Another innovative concept involves forward-facing jet injection from the blunt bodies with and without upstream energy deposition. Numerical examinations conducted by Marley and Riggins (2011) reveal that, drag and heat reduction can be achieved by injecting a fluid centrally or near the stagnation point. Gases tested include air, nitrogen, helium and also combustible gases like hydrogen. Depending on the freestream and jet conditions, heat and drag reductions of up to 40% could be attained. Investigations show that there are two modes of injection. In the first mode, due to the low pressure the jet does not penetrate through the bow shock formed in front of the blunt body. Instead, it pushes the shock away from the blunt body. Although it does not alter the pressure drag significantly, it increases the boundary layer, thus, substantially reducing the heat transfer to the surface. As the ratio of the total pressure to the freestream total pressure increases, a second mode is achieved. In this mode, the jet penetrates the shock, decelerates and

turns itself until there is a match in the total pressure in the regions. This produces results similar to a physical spike and can be used to replace it. Recirculation regions form adjacent to the jet downstream of the jet induced shock. It is necessary to monitor the jet and freestream conditions to prevent the jet induced shock from impinging on the blunt body and create regions of adverse pressure gradient and high heat flux. It is also observed that both the modes of jet injection are unstable and change from one mode to another in a cyclic manner. A Viscous Upwind Algorithm for Complex Flow Analysis (VULCAN) CFD solver developed at NASA Langley Research center was used for numerical analysis. Energy deposition achieved using electronic beams was used for partial stabilization of jet. Another technique tested to stabilize the jet was centered swirl injection of jet. It was found that swirl injection induces axisymmetric flow around the jet and causes pressure variations on its sides. This makes the jet more unstable. A ring injection case was also tested. The jet is more stabilized in this case when compared to the swirl injection, the reason being, the jet on either side is isolated due to the void in the center of the ring. However, a slight pressure decrease in one region may disrupt the symmetry, resulting in destabilizing the jet (Marley and Riggins, 2011).
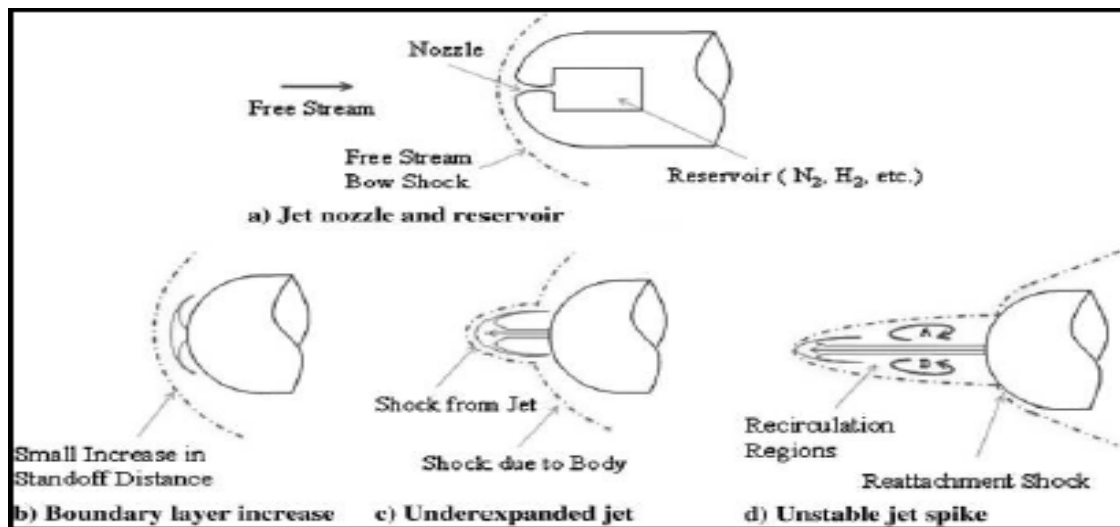

Figure 1.7. a) Sketches of injector nozzle and reservoir; b)-d) distinct modes of injection (Marley and Riggins, 2011)

Numerical studies conducted by Aruna and Anjalidevi(2013) show that forward facing jet injection can be applied to tangent ogive nosecones as well as blunt bodies.

Higher jet injection pressures are required to produce larger reductions in drag and heat transfer in hypersonic nose cones.

Numerical studies have been performed by Liu and Jiang(2013) to study the spike-lateral jet concept. The experiment is described in section 1.3.1. Axisymmetric and three dimensional compressible Navier-Stokes equations were solved along with the Spalart-Almaras one equation model to simulate turbulence. The convective terms were solved by second order schemes, viscous fluxes using second order central differencing and Steger-Warming flux vector splitting for upwind effects. The simulations were done with the assumption of an isothermal, impermeable non-slip wall. Two cases were tested; one at zero degree angle of attack and the other at 4 degree angle of attack to account for the off- design effects. Results apparently show that shock impingement on the blunt body is avoidable at off-design conditions on the windward side, as the reattachment point is pushed further. However, shock impingement is unavoidable on the leeward side. The peak heat transfer rate at the reattachment point is proportional to the peak pressure. With the use of lateral jets, it was shown that the peak pressure could be reduced by 65% using lateral jets. Moreover, the advantage of using a pure blunt body was seen. Higher heat reduction rates were achieved with pure blunt body shapes (Liu and Jiang, 2013).

In this thesis, the concept of spike-lateral jet combination is studied. The thesis is organized as follows,

- In Chapter 2 we discuss the physical problem
- Chapter 3 explains the approach used to solve the physical problem.
- Chapter 4 enumerates all the governing equations required.
- Chapter 5 gives an outline of the four test cases and inputs required for each case.
- Chapter 6 describes the results of all test cases and compares it with the journal article published by Liu and Jiang(2013).
- Chapter 7 elucidates the conclusion obtained by analyzing all the test results.

2. Problem Statement

The objective of this thesis project is to numerically investigate the new Non-Ablative Thermal Protection system (NaTPS) concept the spike-lateral jet combination. The project focuses on visualizing the complex flow structure at high speeds, the shock-shock interactions created due to the presence of spike and jets including the shock wave-boundary layer interactions. The reduction in the drag and heat flux is measured by comparing the results with and without the presence of jets. All previous researches done use the Spalart-Allmaras one equation model to simulate turbulence effects on the boundary layer and re-circulating regions. In this project, the k-ω two-equation turbulence model has been used to model the case.

The geometry used is that of the studies conducted by Liu and Jiang (2013). The test model specifications are given in Chapter 6. The flow conditions are also identical to that used by Liu and Jiang (2013). These values were selected to compare the results for the two turbulence models: Spalart Allmaras model used in Liu and Jiang (2013) and the k-ω model used in this thesis.

The flow conditions used in this thesis are:

- Freestream Mach number 6; with standard atmospheric conditions at 30km altitude i.e. static temperature of 231.24 K, static pressure of 1357 Pa.
- Jet Mach number 2.2 injected with static pressure of 47383.55 Pa and temperature 151.423 K
- An isothermal no-slip surface at a temperature of 500K

The following assumptions are made to simplify the complexity in modeling the spike-jet concept:

- Even though the studies conducted by Liu and Jiang (2013) compare efficiencies of the jet at zero and 4 degree angles of attack, plots for numerical results for heat transfer in the journal article by Liu and Jiang (2013), are presented only for zero

degree angle of attack. Hence for validation, the angle of attack in this project is assumed to be zero.

- The flow is chemically frozen.
- Radiation is negligible.

3.   Approach

The computation of the flow field involves solution of compressible Navier-Stokes equations using an in-house research code called HYP. It is a lower order, compressible Fortran 90 MPI parallel multiblock code. The Wilcox k-ω model was recently implemented in the code and was applied to 2D cases by Horvath(2010). The 2D test cases have been explained in Chapter 4. This code was chosen to test its functionality for 3D cases.

Steger Warming Flux vector splitting described in Steger and Warming (1979) will be employed to capture the shocks because it is appropriate for hypersonic flows. The central differencing method will be used for viscous fluxes. The Wilcox k-ω model will be used for modeling turbulence in the flow. The geometry will be created in CATIA V5 and meshed in Pointwise. The Gridgen software will be utilized for applying boundary conditions, because it is compatible with the code. The post-processing will be done in TecPlot 360.

4. Governing Equations

Much of the present day computational research on turbulent flows is done through Reynolds-averaged Navier-Stokes equations (RANS). The RANS equations are derived by converting the dependent variables in the conservation equations into time-mean and fluctuating components. The fluctuating components are interpreted as apparent stresses and heat fluxes related to turbulent eddies. These new quantities must be related to the mean flow variables through the turbulent models.

The conservation form of RANS and turbulence model equation can be written in Cartesian coordinates as follows:

$$\frac{\partial Q}{\partial t} + \frac{\partial}{\partial x}(F_I - F_V) + \frac{\partial}{\partial y}(G_I - G_V) + \frac{\partial}{\partial z}(H_I - H_V) = S \qquad (4.1)$$

These equations are transformed into computational space (ξ, η, ζ) for solution. The transformed equation is:

$$\frac{\partial Q}{\partial t} + \frac{\partial}{\partial \xi}(F'_I - F'_V) + \frac{\partial}{\partial \eta}(G'_I - G'_V) + \frac{\partial}{\partial \zeta}(H'_I - H'_V) = S \qquad (4.2)$$

When using this transformation, the conservation state vector (Q) remains the same for both the physical and computational domains. It is given as,

$$Q = \begin{bmatrix} \overline{\rho} \\ \overline{\rho u} \\ \overline{\rho v} \\ \overline{\rho w} \\ \overline{\rho E} \\ \overline{\rho k} \\ \overline{\rho \omega} \end{bmatrix} \qquad (4.3)$$

The difference between the physical and computational domains is mainly noticed in the flux vector and the source terms. The flux vectors may be split into inviscid and viscous types which are discussed below.

4.1 Inviscid Fluxes

The inviscid flux vectors in (x,y,z) plane are given by,

$$F_I = \begin{bmatrix} \overline{\rho u} \\ \overline{\rho u}^2 + P + \frac{2}{3}\overline{\rho k} \\ \overline{\rho u v} \\ \overline{\rho u w} \\ \overline{u}\left(\overline{\rho E} + P + \frac{2}{3}\overline{\rho k}\right) \\ \overline{\rho u k} \\ \overline{\rho u \omega} \end{bmatrix} \quad G_I = \begin{bmatrix} \overline{\rho v} \\ \overline{\rho v u} \\ \overline{\rho v}^2 + P + \frac{2}{3}\overline{\rho k} \\ \overline{\rho v w} \\ \overline{v}\left(\overline{\rho E} + P + \frac{2}{3}\overline{\rho k}\right) \\ \overline{\rho v k} \\ \overline{\rho v \omega} \end{bmatrix} \quad H_I = \begin{bmatrix} \overline{\rho w} \\ \overline{\rho w u} \\ \overline{\rho w v} \\ \overline{\rho w}^2 + P + \frac{2}{3}\overline{\rho k} \\ \overline{w}\left(\overline{\rho E} + P + \frac{2}{3}\overline{\rho k}\right) \\ \overline{\rho w k} \\ \overline{\rho w \omega} \end{bmatrix} \quad (4.4)$$

In Eq. (5.4), the pressure like term $\frac{2}{3}\overline{\rho k}$ is a component of Reynolds Stress tensor. As it is a first derivative in the system of equations, it belongs to the inviscid fluxes. A transformation needs to be done to find the flux vectors in the computational space.

$$F' = \xi_x F + \xi_y G + \xi_z H \qquad G' = \eta_x F + \eta_y G + \eta_z H \qquad H' = \zeta_x F + \zeta_y G + \zeta_z H \quad (4.5)$$

In the Eq. (5.5), $\xi_x = \frac{\partial \xi}{\partial x}$ for example are called metrics, which are determined by grid geometry. The velocities in the computational domain are also found using a similar transformation. After transformation, the inviscid flux vector is given by Eq.(5.6). The inviscid flux vectors in the η and ζ directions can be obtained in an identical way with exception for velocities and metrics.

$$F_I' = \begin{bmatrix} \overline{\rho \overline{u}}' \\[6pt] \overline{\rho u \overline{u}}' + \xi_x\left(\frac{2}{3}\overline{\rho k} + P\right) \\[6pt] \overline{\rho v \overline{u}}' + \xi_y\left(\frac{2}{3}\overline{\rho k} + P\right) \\[6pt] \overline{\rho w \overline{u}}' + \xi_z\left(\frac{2}{3}\overline{\rho k} + P\right) \\[6pt] \left(\overline{\rho E} + P + \frac{2}{3}\overline{\rho k}\right)\overline{u}' \\[6pt] \overline{\rho k \overline{u}}' \\[6pt] \overline{\rho \omega \overline{u}}' \end{bmatrix} \tag{4.6}$$

Steger-Warming Flux vector splitting is used to upwind the inviscid fluxes. While upwinding, only the information from the domain of dependence is used to discretize the fluxes, hence it can be applied to all flow regimes. The following procedure illustrates the Steger-Warming method.

The Euler equations in the computational domain are given by,

$$\frac{\partial Q}{\partial t} + A\frac{\partial Q}{\partial \xi} + B\frac{\partial Q}{\partial \eta} + C\frac{\partial Q}{\partial \zeta} = 0 \tag{4.7}$$

A, B and C are the conservative flux jacobians expressed as,

$$A = \frac{\partial F'}{\partial Q} \qquad B = \frac{\partial G'}{\partial Q} \qquad C = \frac{\partial H'}{\partial Q} \tag{4.8}$$

The flux vectors are considered as homogeneous functions of degree one in Q, if the perfect gas condition is valid. Hence, flux vectors can be expressed as,

$$F' = AQ \quad G' = BQ \quad H' = CQ \tag{4.9}$$

A flux jacobian can be decomposed into its eigenvectors as follows:

$$A = R\Lambda L \tag{4.10}$$

In Eq. (4.10), L is the matrix of left eigenvectors given by the inverse of right eigenvectors(R). In the flux vector splitting method, the positive and the negative fluxes are separated using the respective eigenvalues in the calculation.

$$F' = F'^{+} + F'^{-} = R\Lambda^{+}LQ + R\Lambda^{-}LQ \qquad (4.11)$$

The eigenvalues of F'^{+} positive and the eigenvalues of F'^{-} are negative. They can be found by recasting the equations into primitive system. The equations may then be upwinded to find various cell values. Here, only an introduction to the procedure is given. The derivation can be found in Hirsch (1990). The explicit upwind scheme used here is of first order. (Horvath, 2010)

The use of split flux techniques for shock capturing produces better results when compared to central difference methods, but some problems occur even in this formulation. In Steger Warming method, the shocks are well represented, but oscillations are produced at sonic conditions. The problem is that the split flux components become discontinuous at the sonic and the stagnation points. To eliminate this problem, the eigen values are modified as,

$$\lambda^{\pm} = \frac{\lambda \pm \sqrt{\lambda^{2} + \varepsilon^{2}}}{2} \qquad (4.12)$$

where, ε is viewed as a blending function to ensure smooth transition when the eigenvalues change sign (Pletcher, Tannehill and Anderson, 2013, p 374-379).

4.2   Viscous fluxes

The viscous fluxes in the (x,y,z) directions are given by the following equations. Central differencing method of second order is used to discretize the derivative terms.

$$F_v = \begin{bmatrix} 0 \\ 2\overline{S_{xx}}(\mu + \mu_T) \\ 2S_{xy}(\mu + \mu_T) \\ 2S_{xz}(\mu + \mu_T) \\ \left(\kappa + \dfrac{\mu_T C_P}{\mathrm{Pr}_T}\right)\dfrac{\partial \overline{T}}{\partial x} + \left(\mu + \sigma^*\dfrac{\overline{\rho k}}{\omega}\right)\dfrac{\partial k}{\partial x} + 2(\mu + \mu_T)\left(\overline{u\,S_{xx}} + \overline{v}S_{xy} + \overline{w}S_{xz}\right) \\ \left(\mu + \sigma^*\dfrac{\overline{\rho k}}{\omega}\right)\dfrac{\partial k}{\partial x} \\ \left(\mu + \sigma^*\dfrac{\overline{\rho k}}{\omega}\right)\dfrac{\partial \omega}{\partial x} \end{bmatrix} \qquad (4.13)$$

$$G_V = \begin{bmatrix} 0 \\ 2S_{yx}(\mu + \mu_T) \\ 2\overline{S_{yy}}(\mu + \mu_T) \\ 2S_{yz}(\mu + \mu_T) \\ \left(\kappa + \dfrac{\mu_T C_P}{\mathrm{Pr}_T}\right)\dfrac{\partial \overline{T}}{\partial y} + \left(\mu + \sigma^*\dfrac{\overline{\rho k}}{\omega}\right)\dfrac{\partial k}{\partial y} + 2(\mu + \mu_T)\left(\overline{u}S_{yx} + \overline{v\,S_{yy}} + \overline{w}S_{yz}\right) \\ \left(\mu + \sigma^*\dfrac{\overline{\rho k}}{\omega}\right)\dfrac{\partial k}{\partial y} \\ \left(\mu + \sigma^*\dfrac{\overline{\rho k}}{\omega}\right)\dfrac{\partial \omega}{\partial y} \end{bmatrix} \qquad (4.14)$$

$$
H_V = \begin{bmatrix}
0 \\
2S_{yx}(\mu + \mu_T) \\
2\overline{S_{yy}}(\mu + \mu_T) \\
2S_{yz}(\mu + \mu_T) \\
\left(\kappa + \dfrac{\mu_T C_P}{\mathrm{Pr}_T}\right)\dfrac{\partial \overline{T}}{\partial z} + \left(\mu + \sigma^* \dfrac{\overline{\rho k}}{\omega}\right)\dfrac{\partial k}{\partial z} + 2(\mu + \mu_T)\left(\overline{u}S_{zx} + \overline{v}S_{zy} + \overline{w}\overline{S_{zz}}\right) \\
\left(\mu + \sigma^* \dfrac{\overline{\rho k}}{\omega}\right)\dfrac{\partial k}{\partial z} \\
\left(\mu + \sigma^* \dfrac{\overline{\rho k}}{\omega}\right)\dfrac{\partial \omega}{\partial z}
\end{bmatrix}
\tag{4.15}
$$

Previously used transformations can be used to convert the viscous fluxes in the physical plane to the computational plane. The viscous flux vector in the ξ plane is given by,

$$
F_V{}' = \begin{bmatrix}
0 \\
2(\mu + \mu_T)\left(\xi_x \overline{S}_{xx} + \xi_y S_{yx} + \xi_z S_{zx}\right) \\
2(\mu + \mu_T)\left(S_{xy} + \xi_y \overline{S}_{yy} + \xi_z S_{zy}\right) \\
2(\mu + \mu_T)\left(\xi_x S_{xz} + \xi_y S_{yz} + \xi_z \overline{S}_{zz}\right) \\
\left(\kappa + \dfrac{\mu_T C_P}{\mathrm{Pr}_T}\right)\dfrac{\partial \xi}{\partial x}\dfrac{\partial \overline{T}}{\partial x} + \left(\mu + \sigma^* \dfrac{\overline{\rho k}}{\omega}\right)\dfrac{\partial \xi}{\partial x}\dfrac{\partial k}{\partial x} + 2(\mu + \mu_T)\dfrac{\partial \xi}{\partial x}\left(\overline{u}\overline{S_{xx}}\right) \\
\left(\mu + \sigma^* \dfrac{\overline{\rho k}}{\omega}\right)\left(\xi_x \dfrac{\partial k}{\partial x} + \xi_y \dfrac{\partial k}{\partial y} + \xi_z \dfrac{\partial k}{\partial z}\right) \\
\left(\mu + \sigma^* \dfrac{\overline{\rho k}}{\omega}\right)\left(\xi_x \dfrac{\partial k}{\partial x} + \xi_y \dfrac{\partial k}{\partial y} + \xi_z \dfrac{\partial k}{\partial z}\right)
\end{bmatrix}
\tag{4.16}
$$

The transformed viscous fluxes in the other two directions of the computational plane can be written in a similar manner.

4.3   Source Terms

The source terms here occur only due to turbulence terms. It can be expressed as,

$$
S = \begin{bmatrix}
0 \\
0 \\
0 \\
0 \\
0 \\
\bar{\tau}_T \dfrac{\partial \bar{u}}{\partial x} - \beta^* \bar{\rho} k \omega \\
\alpha \dfrac{\omega}{k} \bar{\tau}_T \dfrac{\partial \bar{u}}{\partial x} - \beta \bar{\rho} \dfrac{\partial k}{\partial x} \dfrac{\partial \omega}{\partial x}
\end{bmatrix}
\tag{4.17}
$$

(Horvath, 2010).

4.4   Wilcox k-ω Turbulence Model

The model illustrated here is the Wilcox k-ω model, version 2006. The k-ω model is a two-equation turbulence model that uses turbulent kinetic energy equation and the specific dissipation rate equations to predict properties of turbulent flow. The turbulent kinetic energy equation is derived by multiplying the instantaneous momentum equation by the fluctuating component of velocity (u_i'') followed by time averaging. The equation obtained after doing considerable amount of algebra is given below.

$$
\frac{\partial(\bar{\rho}k)}{\partial t} + \frac{\partial(\bar{\rho}\bar{u}_j k)}{\partial x_j} = \bar{\tau}_{T_{ij}} \frac{\partial \bar{u}_i}{\partial x_j} - \overline{\tau_{L_{ji}} \frac{\partial u_i''}{\partial x_j}} + \frac{\partial}{\partial x_j}\left(\overline{\tau_{L_{ji}} u_i''} - \overline{\rho u_j'' \frac{1}{2} u_i'' u_i''} - \overline{p' u_j''} \right) - \overline{u_i''} \frac{\partial P}{\partial x_i} + \overline{p' \frac{\partial u_i''}{\partial x_i}}
\tag{4.18}
$$

In Eq. (5.18), the terms on the left hand side are unsteady and convective terms. The first term on right hand side represents the rate of transfer of energy from the mean flow to

turbulence which gives the turbulence energy per unit volume. The second term shows the rate of change of kinetic energy to heat termed as dissipation, which is modeled as,

$$\overline{\tau_{L_{ji}} \frac{\partial u_i''}{\partial x_j}} = \beta^* \overline{\rho} k \omega \tag{4.19}$$

The third and fourth terms represent molecular diffusion and turbulent transport of turbulent kinetic energy. The final three terms are pressure diffusion, pressure work and pressure dilatation. The pressure work and pressure dilatation terms are useful for large turbulence production to dissipation ratio especially in cross flows. However, when modeling boundary layer flows, these terms can be neglected. The turbulent kinetic energy equation for this case can be written as,

$$\frac{\partial (\overline{\rho} k)}{\partial t} + \frac{\partial (\overline{\rho u_j} k)}{\partial x_j} = \overline{\tau_{T_{ij}}} \frac{\partial \overline{u_i}}{\partial x_j} - \beta^* \overline{\rho} k \omega + \frac{\partial}{\partial x_j}\left[\left(\mu + \sigma^* \frac{\overline{\rho} k}{\omega}\right) \frac{\partial k}{\partial x_j}\right] \tag{4.20}$$

The specific dissipation rate cannot be derived. Hence, it is assumed to have similar form with unsteadiness, convection, production, diffusion and dissipation. The specific dissipation rate equation is expressed as follows,

$$\frac{\partial (\overline{\rho} \omega)}{\partial t} + \frac{\partial (\overline{\rho u_j} \omega)}{\partial x_j} = \alpha \frac{\omega}{k} \overline{\tau_{T_{ij}}} \frac{\partial \overline{u_i}}{\partial x_j} - \beta \overline{\rho} \omega^2 + \frac{\partial}{\partial x_j}\left[\left(\mu + \sigma^* \frac{\overline{\rho} k}{\omega}\right) \frac{\partial \omega}{\partial x_j}\right] + \sigma_d \frac{\overline{\rho}}{\omega} \frac{\partial k}{\partial x_j} \frac{\partial \omega}{\partial x_j} \tag{4.21}$$

The supplementary equations and the closure coefficient used in all above equations are defined here. The laminar shear stress and the Reynolds stress tensors obtained by Boussinesq approximation are also shown here.

$$\overline{\tau_{L_{ij}}} = 2\mu \overline{S_{ij}} \qquad \overline{\tau_{T_{ij}}} = 2\mu \overline{S_{ij}} - \frac{2}{3} \overline{\rho} k \delta_{ij} \qquad \overline{S_{ij}} = S_{ij} - \frac{1}{3} \frac{\partial \overline{u_k}}{\partial x_k} \delta_{ij} \tag{4.22}$$

The mean strain rate tensor and the Kronecker delta are defined as,

$$S_{ij} = \frac{1}{2}\left(\frac{\partial \overline{u_i}}{\partial x_j} + \frac{\partial \overline{u_j}}{\partial x_i}\right) \qquad \delta_{ij} = \begin{Bmatrix} 1, i = j \\ 0, i \neq j \end{Bmatrix} \tag{4.23}$$

The eddy viscosity can also be calculated using Boussinesq approximation as,

$$\mu_T = \frac{\overline{\rho}k}{\overline{\omega}} \qquad \overline{\omega} = \max\left\{\omega, C_{\lim}\sqrt{\frac{2\overline{S_{ij}\,S_{ij}}}{\beta^*}}\right\} \qquad C_{\lim} = \frac{7}{8} \tag{4.24}$$

The eddy viscosity is limited by the stress limiter in the denomination of Eq. (5.24). The expressions for laminar and turbulent heat fluxes are,

$$q_{L_j} = -\kappa\frac{\partial \overline{T}}{\partial x_j} \qquad\qquad q_{T_j} = -\frac{\mu_T C_P}{Pr_T}\frac{\partial \overline{T}}{\partial x_j} \tag{4.25}$$

The closure coefficients and constants in the equations are given by the following expressions,

$$\alpha = \frac{13}{25} \qquad \beta^* = \frac{9}{100} \qquad \sigma = \frac{1}{2} \qquad \sigma^* = \frac{3}{5} \qquad Pr_T = \frac{8}{9} \tag{4.26}$$

$$\sigma_d = \begin{cases} 0, & \dfrac{\partial k}{\partial x_j}\dfrac{\partial \omega}{\partial x_j} \le 0 \\[2mm] \dfrac{1}{8}, & \dfrac{\partial k}{\partial x_j}\dfrac{\partial \omega}{\partial x_j} > 0 \end{cases} \tag{4.27}$$

$$\beta = 0.0708 f_\beta \qquad f_\beta = \frac{1+85\chi_\omega}{1+100\chi_\omega} \qquad \chi_\beta = \left|\frac{\Omega_{ij}\Omega_{jk}\hat{S}_{kj}}{\left(\beta^*\omega\right)^3}\right| \tag{4.28}$$

$$\Omega_{ij} = \frac{1}{2}\left(\frac{\partial \overline{u}_i}{\partial x_j} - \frac{\partial \overline{u}_j}{\partial x_i}\right) \qquad\qquad \hat{S}_{kj} = S_{kj} - \frac{1}{2}\frac{\partial \overline{u}_m}{\partial x_m}\delta_{kl} \tag{4.29}$$

The RANS equation along with the turbulent model equations form the complete set of equations required to simulate turbulent flows (Horvath, 2010; Wilcox, 2006).

4.4.1   k-ω Turbulence Model Test Cases

The k-ω Turbulence Model was installed and tested by Horvath(2010). The test cases are:

- Mach 2.5 flow past a Backward-Facing Step

- Mach 2.85 Flow past a Compression Corner

4.4.1.1 Mach 2.5 flow past a Backward-Facing Step

The case of backward facing step with a step height of 0.443 inches was selected from the NPARC Alliance Verification and Validation Archive. The flow assumes air to be a two-species mixture comprising of 79% N_2 and 21% O_2. The freestream condition include a temperature of 153 K, pressure of 13316 Pa, turbulent kinetic energy 0.00384 m^2/s^2 and a specific dissipation rate of 3900 s^{-1}. The results obtained are compared with those obtained from Wind-US using HLLC scheme and the Menter SST Turbulence Model with compressibility corrections and Cobalt with Wilcox(1998) k-ω model. The results from the HYP code are closest to the Wind-US solver. When the percentage errors are analyzed, all solvers have greater than 5% error for a length of 1.5 inches behind the step. Except at the position of x=2 inches, the HYP code performs equally well in all other regions when compared to the Wind-US code (Horvath,2010).
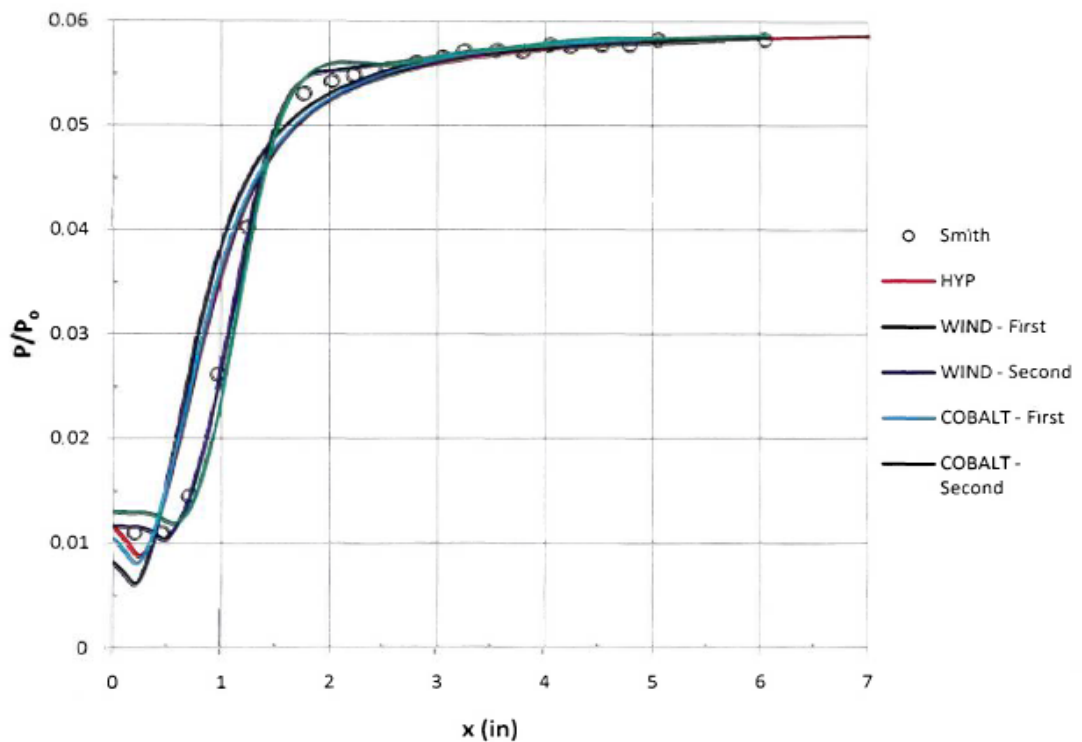

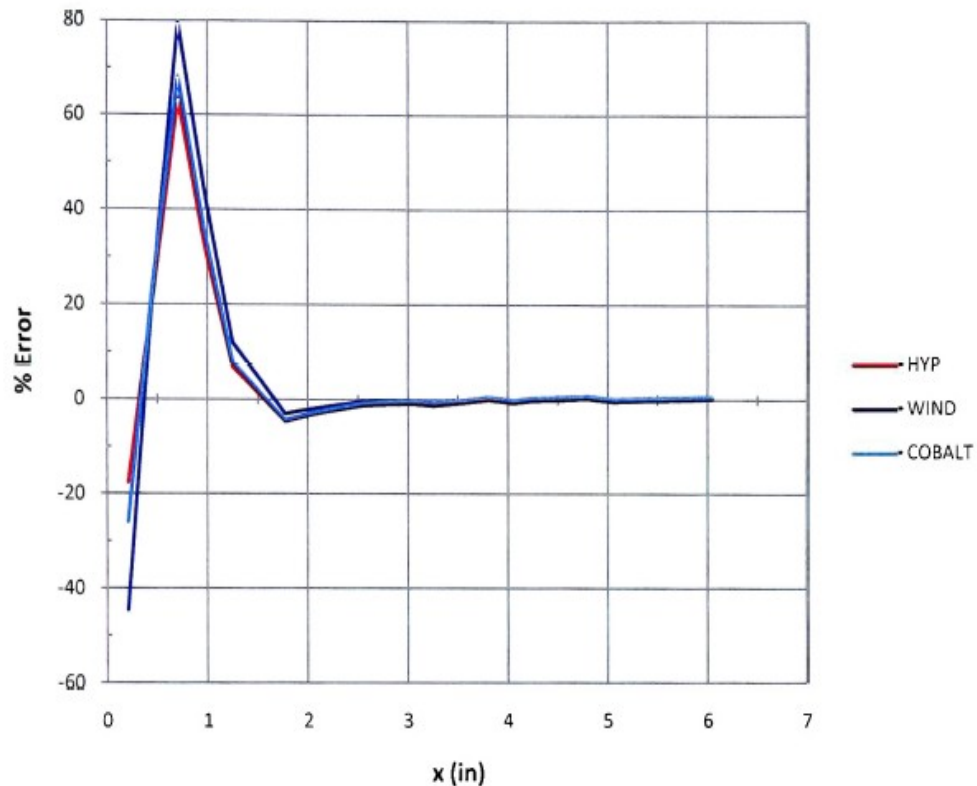Figure 4.1. Surface Pressure-Backward facing Step (Horvath,2010)

Figure 4.2 Percentage Error-Backward facing Step (Horvath,2010)

4.4.1.2   Mach 2.85 flow past a Compression Corner

The flow with a speed of 571 m/s is a considered past a 24° compression corner. The freestream condition include a temperature of 100 K, pressure of 23545 Pa, turbulent kinetic energy 0.0326 m^2/s^2 and a specific dissipation rate of 3870 s^{-1}. The experimental data from Settles, Vas and Bogdonoff(1976) was used to validate the results of the HYP code. The results obtained from Dolling and Murphy(1983) for Mach number 2.9 were used for comparison in addition to those obtained by Wilcox(2006) with a MacCormack scheme for k-ω model and Fluent with Roe-Flux Difference splitting scheme with Wilcox 1998 k-ω model. An analysis of the results show that the first-order solutions of HYP and Fluent show flow separation further downstream. Wilcox(2006) is more accurate in predicting the separation but Fluent has the least amount of error behind the separation point. For this case, the surface pressure

has an error of 27% at the separation point, and 5% downstream of it. HYP has the maximum error when compared to Wilcox(2006) or Fluent (Horvath,2010).
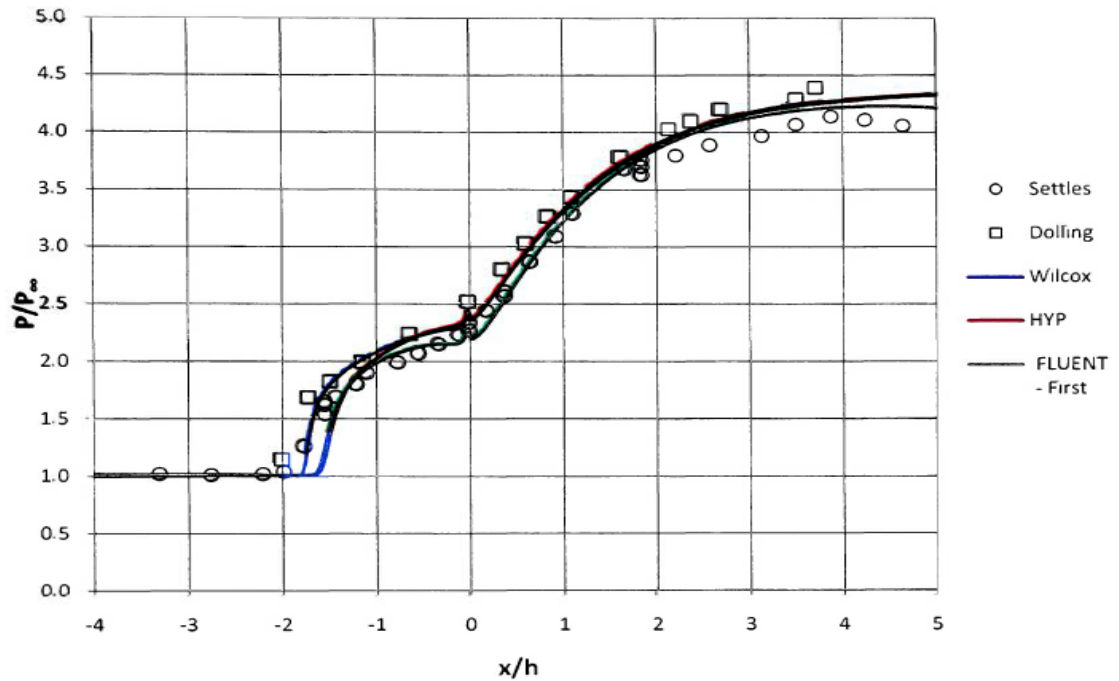

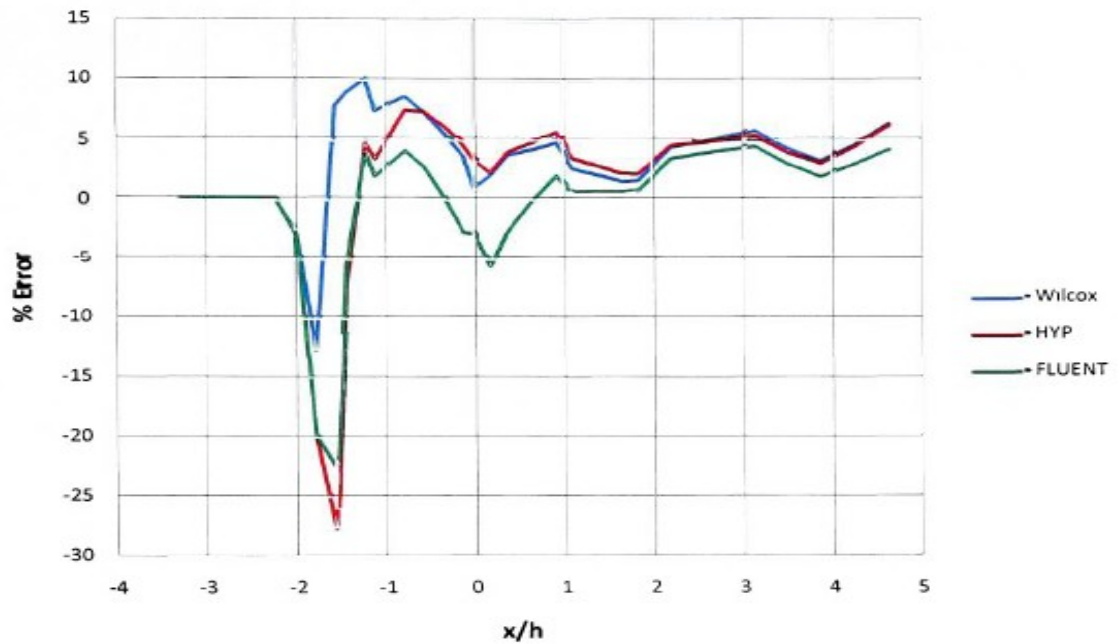Figure 4.3 Surface Pressure-Compression Corner (Horvath,2010)

Figure 4.4 Percent Error-Compression Corner (Horvath,2010)

5. Description of Test Cases

The analysis is conducted for the four test cases: with and without jet injection each modeled for a laminar and a turbulent case. The following sections guide through the development of test cases.

5.1 Modeling and Meshing

The geometry used is that of the studies conducted by Liu and Jiang (2013). The test model specifications are as follows:

- A cylindrical main body of length L = 240mm, D_{outer} = 80mm, D_{inner} = 70mm, with a hemispherical nose.
- Spike attached to the nose has Φ_{outer} = 12mm, Φ_{inner} = 6mm
- Length of the spike is l/D_{outer} =1.0
- Top of the spike is a half-sphere.
- There are two orifices (one on top and the other on bottom). The half-circular[1] orifices of width 1mm are located at 90 degree of the sphere.
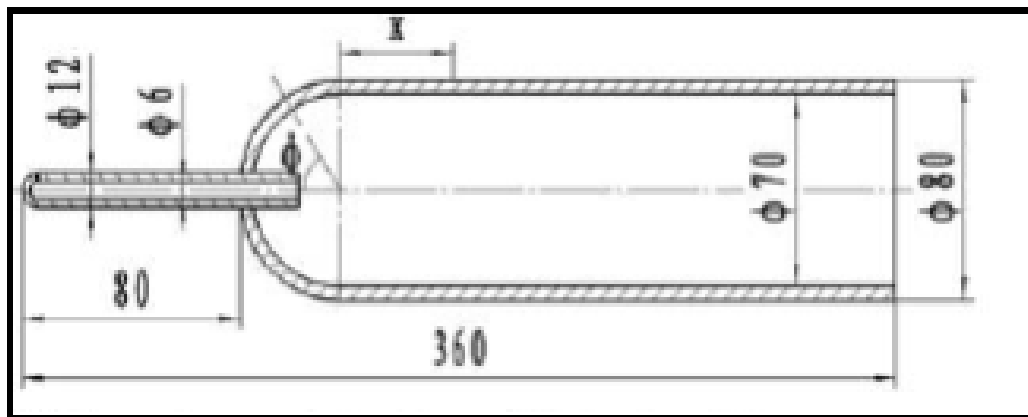

Figure 5.1. Dimensions of the test model (Liu and Jiang, 2013).

---

[1] Although studies conducted by Liu and Jiang (2013) specify a half-circular orifice, the plans supplied by the authors show a circular orifice. The geometry is modeled based on the plans; henceforth the orifice will be referenced as "circular" in this report.

The figure below displays the side view of the aerospike and the circular orifice. This plan was supplied by the authors- Liu and Jiang(2013).
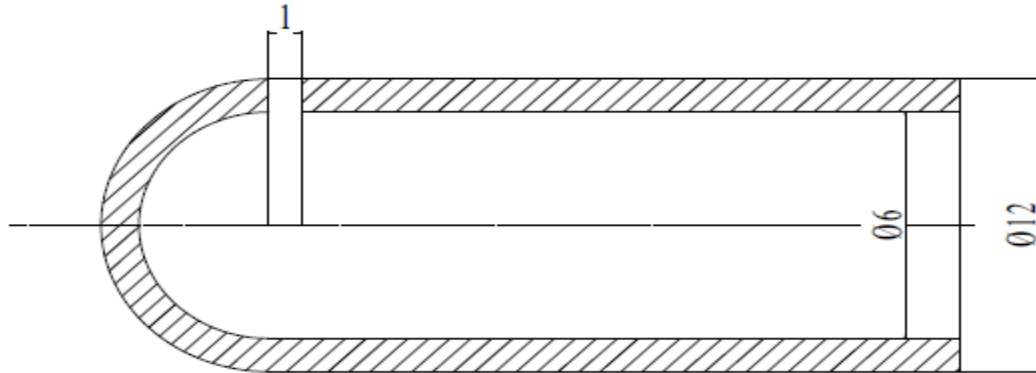

Figure 5.2. Side view of the orifice (Liu and Jiang, 2013).

The spike-blunt body model is created in CATIA V5R20 as per the above mentioned specifications.
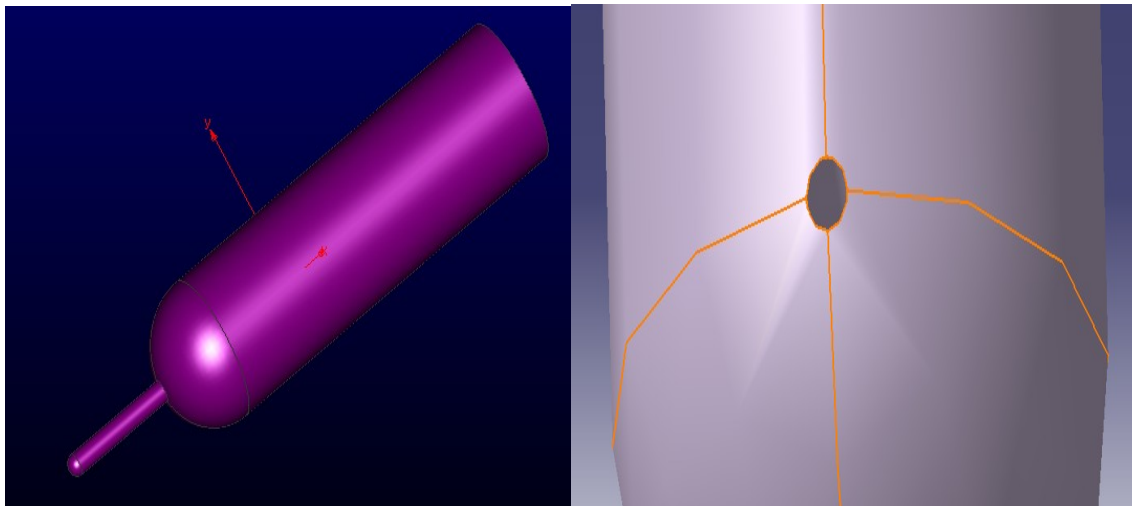

Figure 5.3. Image of the geometry created (left) and zoomed view of orifice (right)

The CATIA model is imported to Pointwise V17.2R1 for meshing. The model has a quarter-plane, hence only a quarter of the geometry is meshed. Thus only half of the

orifice is visualized here. Due to the code's capability of parallel computation, the volume mesh is split into 51 blocks. The number of blocks depends on the process of load balancing i.e. equalizing the number of cells in each block. This increases computational efficiency because each block completes its computation at approximately the same time. The total number of hexahedral cells is 5,235,400 with an approximate number of cells in each block being 125,000. The eight blocks above the circular orifice are the smallest with the number of cells being 14,400. For simplicity, the orifice is not meshed and only the injection plane is set to an inflow or a no-slip wall condition based on the test case. As the region of interest lies near the shoulder of the hemispherical cone, only 60% of the blunt body length is modeled. Thus the total length of the computational domain in the z-direction is 248 mm.
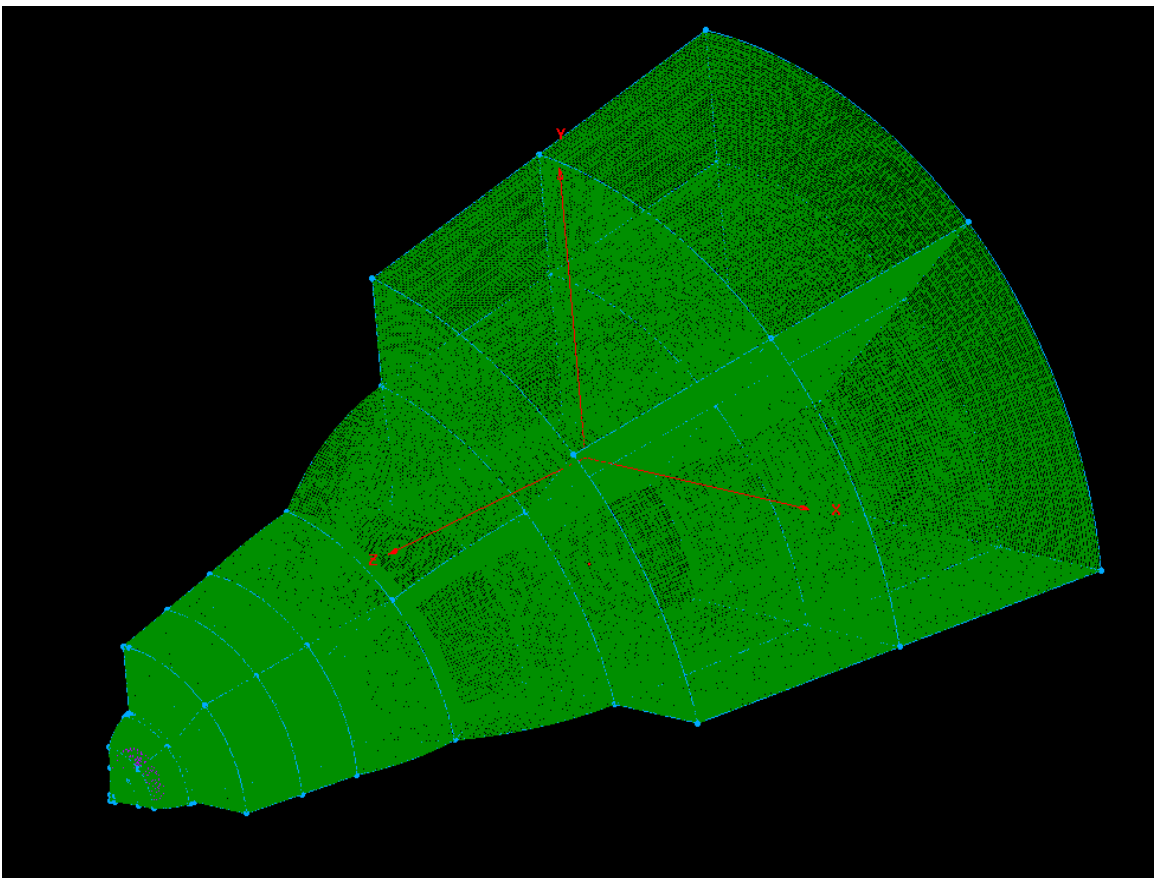

Figure 5.4. Volume mesh showing various blocks.

Grid refinement is necessary to accurately resolve the boundary layer. A good rule of thumb is to use at least 10 grid points within the boundary layer. The boundary layer thickness was calculated with an approximation of a flat plate using the procedure from Holman (2010).

The Reynolds number per unit length for the freestream flow is

$$\text{Re}_x = \frac{\rho v L}{\mu} = \frac{0.0204 \times 1810}{0.00001475} = 2.4542 \times 10^6 \, m^{-1} \qquad (5.1)$$

The length of the spike is 80mm, hence the Reynolds number around the spike is less than 5×10^5 and the flow is laminar.

$$\frac{\delta}{x} = 5.0 \times \text{Re}_x^{-0.5} \qquad (5.2)$$

$$\Rightarrow \boxed{\delta = 0.01128 m^{-1}}$$

Thus, the initial estimate for the grid spacing is 0.001128 m. The dimensionless wall distance (y+) is calculated as an indicator for resolving the boundary layer appropriately while using turbulence models. The y+ value is calculated as described in Wilcox(2006). The wall shear stress (τ_w) is the vector sum of its components in x, y and z-directions. The friction velocity (u_τ) is given by

$$u_\tau = \sqrt{\frac{\tau_w}{\rho}} \qquad (5.3)$$

The spacing y+ is expressed as,

$$y+ = \frac{u_\tau y}{\nu} \qquad (5.4)$$

where, y is the distance of the first grid cell and ν is the kinematic viscosity of the fluid. The y+ calculation is implemented in the code. The contour plots of y+ values for the turbulent cases are shown in the following page.
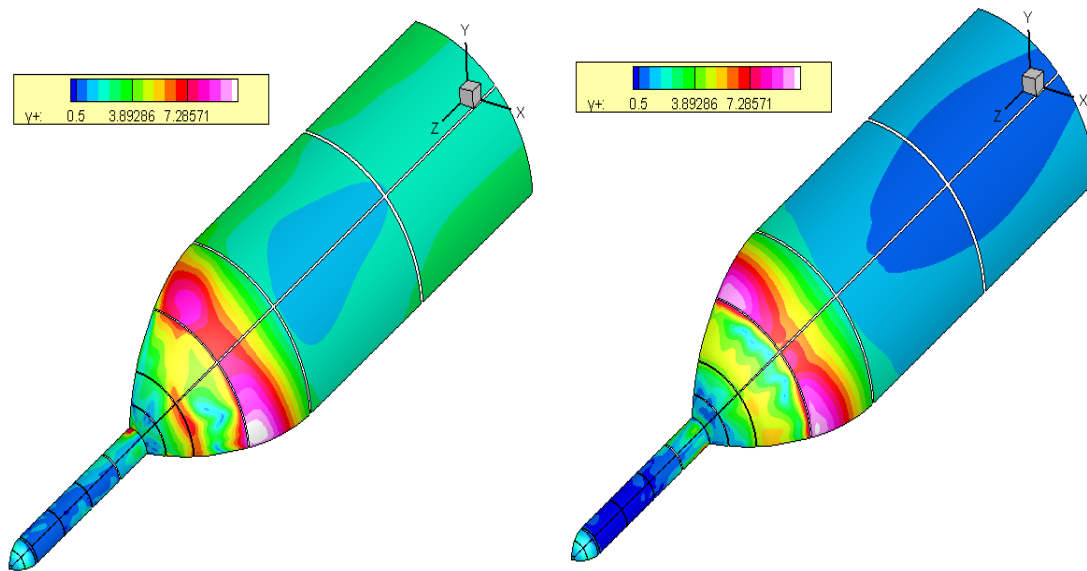
Figure 5.5. y+ values for turbulent cases: with lateral jet injection(left) and without injection(right)

The grid spacing varies from 0.005m near the stagnation point to 0.01m near the orifice, 0.03m on the hemispherical portion of the blunt body with a maximum of 0.84m at the end of the domain. The y+ values are around one or less than one on the spike, but they increase to a maximum of 10.3 for the case with lateral jet injection and 9.4 for the case without injection. This can be seen as red spots on the y+ contour plots. The grid resolves the boundary layer well in other regions of the blunt body and the spike, hence the grid spacing was finalized to the above mentioned values.

5.2   Boundary Conditions

The boundary conditions are applied using Gridgen V15. Five types of boundary conditions are used: supersonic inflow, extrapolation, no-slip wall, symmetry and communication boundary. A supersonic inflow condition indicates that all the information should come from outside the flow domain. An extrapolation boundary condition is used for an outflow boundary. It is a cell-center type boundary condition that extrapolates the values of ghost points from the computational domain. No-slip wall

boundary conditions are used for depicting solid walls where the velocity on the surface goes to zero. A symmetry boundary condition is used on planes where the geometry has a quarter-plane symmetry. The communication boundaries between the blocks are automatically created in Gridgen.
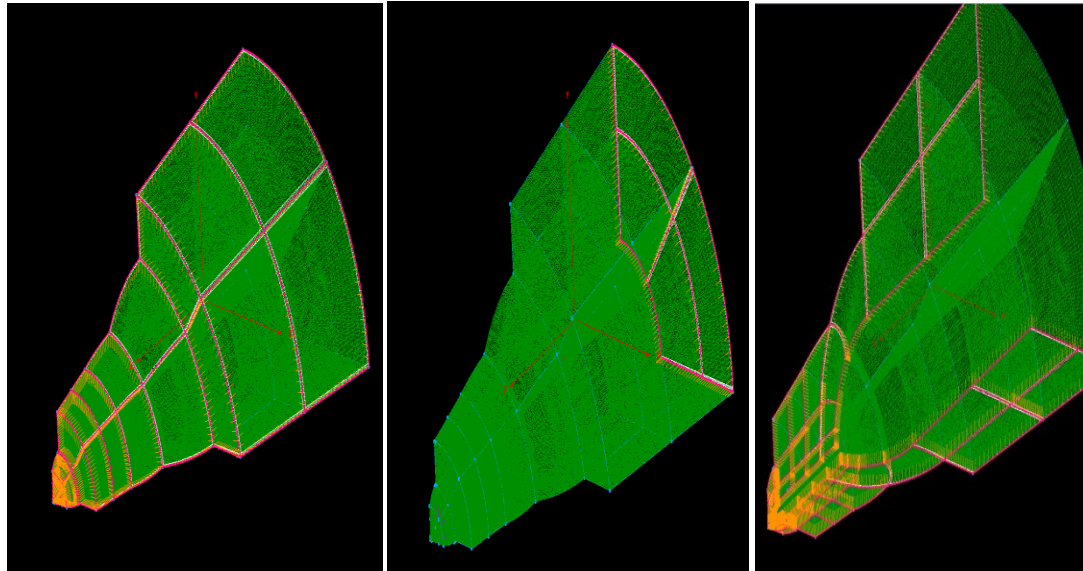

Figure 5.6. Applied boundary conditions: inflow(left), outflow(center) and symmetry(right)

5.3   Test cases and their inputs

5.3.1   Case A: Laminar with Lateral jet injection

This case involves injection of air through the orifice with the assumption of laminar flow. The following table displays various inputs for the case.

Table 5.1. Freestream inputs for all cases

Variables	Input
Pressure	1357 Pa
Temperature	231.24 K
Velocity	1810 m/s
Cfl	0.05

Table 5.2. Orifice inputs

Variables	Input
Pressure	47383.55 Pa
Temperature	151.423 K
Velocity	750 m/s

5.3.2 Case B: Laminar with Non-Injection

In this case, there is no jet injection through the orifice. The inputs for this case are similar to case A, with the exception of velocity at the orifice inlet set to zero.

5.3.3 Case C: Turbulence with Lateral jet injection

The k-ω turbulence model is implemented for the jet injection case. The freestream and the orifice inputs are the same as in case A. Additional inputs required for turbulent model are given in table 5.3. The turbulent kinetic energy and the specific dissipation rate inputs are taken from the test cases by Horvath(2010). They are the values by Wilcox(2006) in the companion software included with the book.

Table 5.3. Inputs for turbulence model

Variables	Input
Turbulent Kinetic energy	0.032761 m^2/s^2
Specific Dissipation Rate	3900 s^{-1}

5.3.4 Case D: Turbulence with Non-injection

The turbulent model is implemented for the non-injection case. The inputs include the values from the tables 5.1 and 5.3.

6. Results and Comparison

The five key concerns that are discussed in this report include: shock-wave reconstruction, heat flux reduction, peak pressure reduction near the blunt body, drag reduction and turbulent model implementation for the spike-jet structure. In the following sections the results are presented and analyzed for each case, and are compared with the numerical results obtained by Liu and Jiang (2013).

6.1 Contour plots for Case A: Laminar with Lateral jet injection

The contour plots for pressure, v-component of velocity, w-component of velocity Mach number, and temperature and heat flux are shown below.
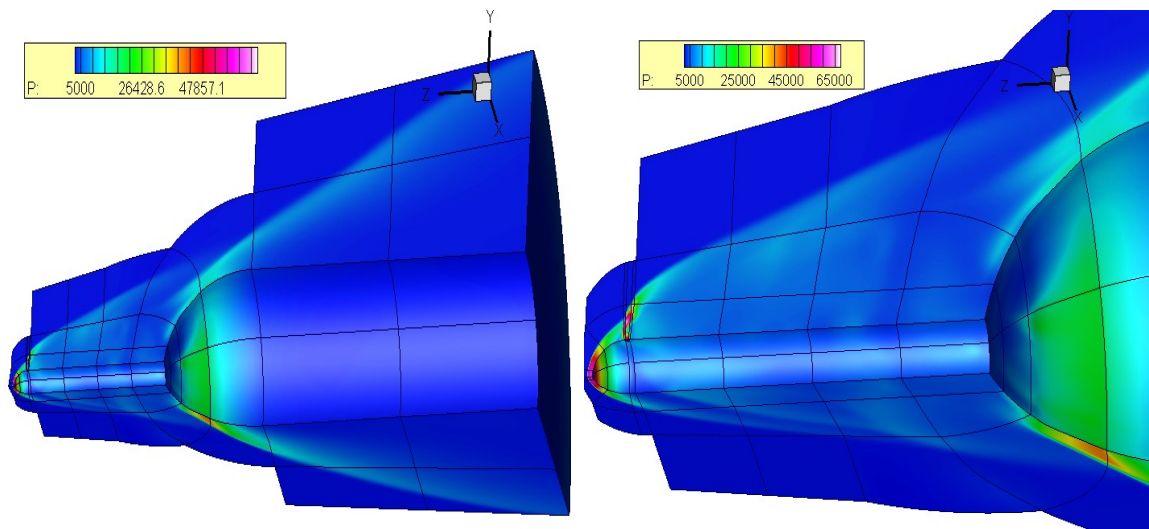
Figure 6.1. Pressure contours for the case A with a zoomed view(right).

The pressure contours reveal the presence of bow shock and conical shock infront of the blunt body and the spike respectively. The stagnation pressure is about 61920 Pa. The peak pressure near the flow reattachment region is around 15500 Pa on the side where the jet is ejected, but on the other side it is around 25000Pa which can be seen as green colored contours on the shoulder of the body in Fig 6.1. Fig 6.2 shows the jet ejected at a velocity of 750m/s in the y-direction. As the ejected jet has enough momentum it pushes

the conical shockwave and enlarges the recirculation region created by the spike. The larger recirculation region and the shock-shock interaction point can be visualized clearly in Fig 6.3.
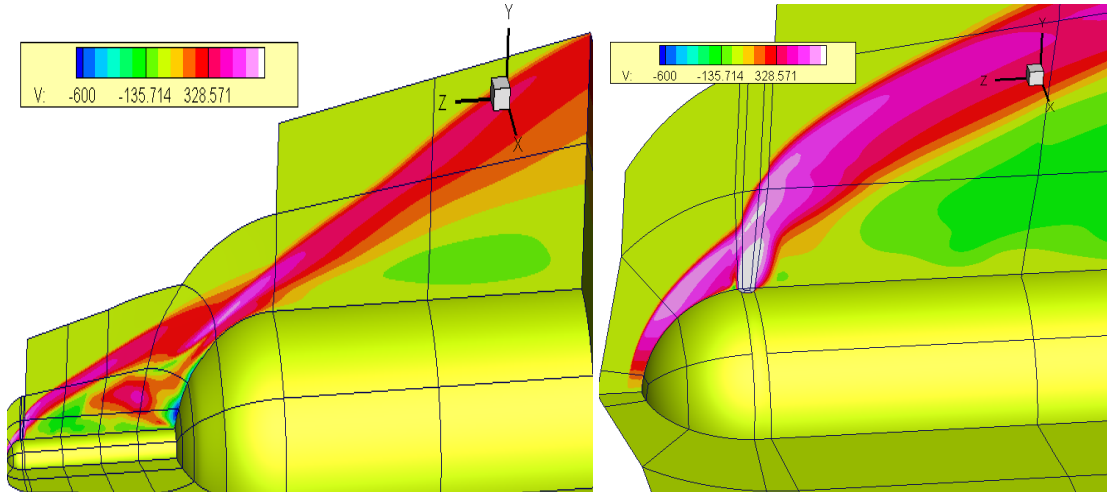

Figure 6.2. Contours for v-component of velocity for case A with zoomed view of jet(right)
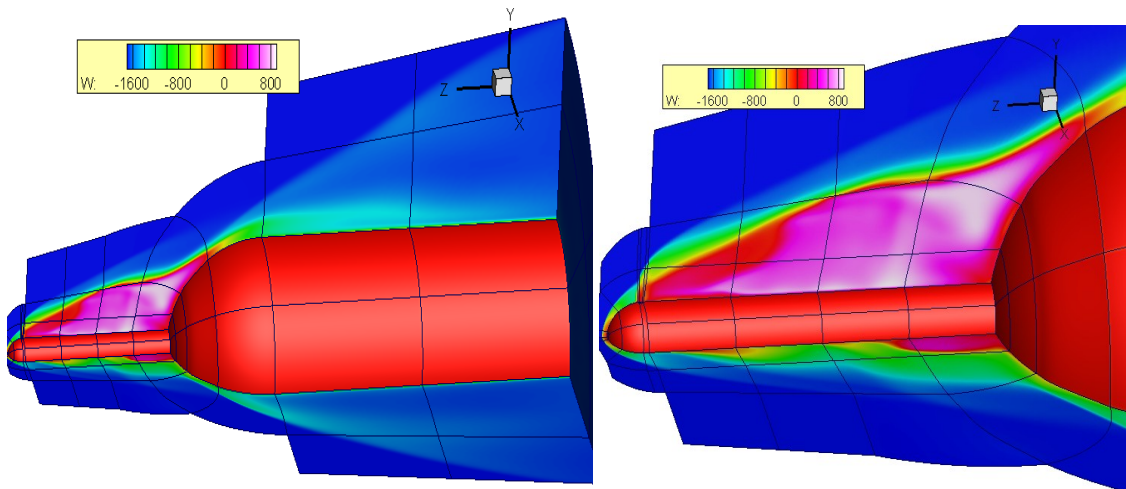

Figure 6.3. Contours for w-component of velocity for case A with zoomed view of recirculation zone(right)

The flow separation shock distinguishes the inviscid free stream layer from the recirculation region. The flow separation shock is visible on the outer boundary of the recirculation zone as dark blue colored lines in Fig 6.4. The Mach number changes from values greater than 1.5 in the freestream to 0.4 in the recirculation region.
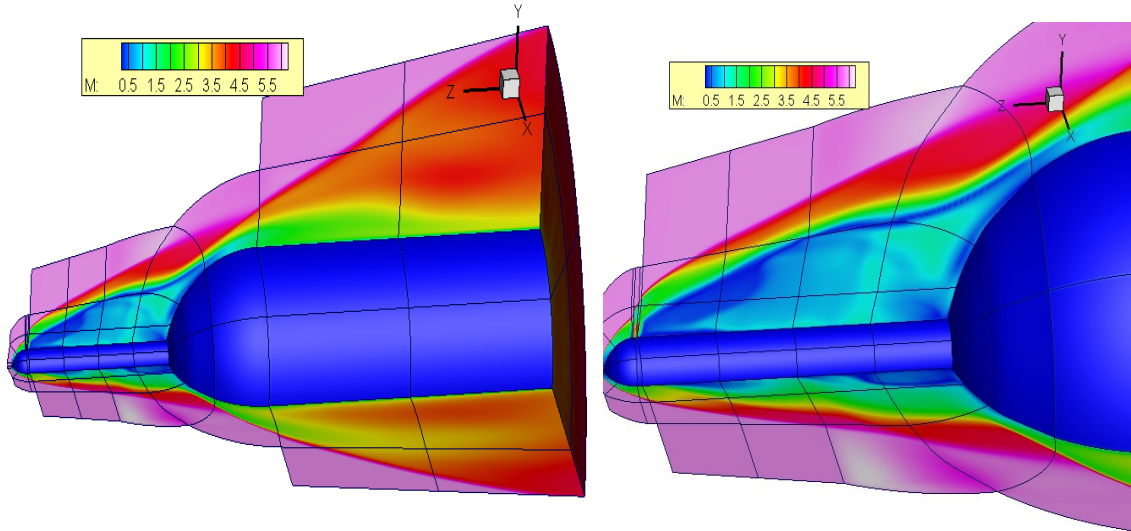
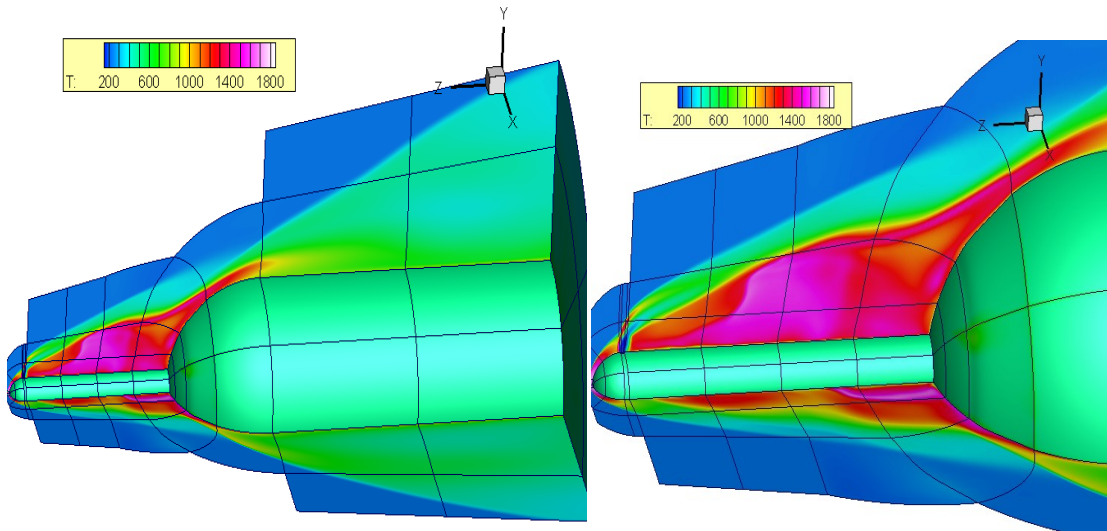Figure 6.4. Mach contours for case A with zoomed view of flow separation shock(right)

Figure 6.5. Temperature contours for case A with zoomed view of high temperature region on the blunt body(right)

The shock-shock interation causes high temperature and high pressure regions on the blunt body. This occurs near the flow reattachment point at the boundary of the recirculation zone. It is observed from Fig 6.5 that the shock-shock interaction point is pushed further backward along the shoulder of the blunt body due to the large recirculation zone. The temperature at the interaction point is reduced to 1340K. The jet reconstructs only a small region of the flow field in front of the blunt body. As a result,

the region of the flow field perpendicular to the jet displays conditions similar to the no-jet case where the temperatures are around 1530K.
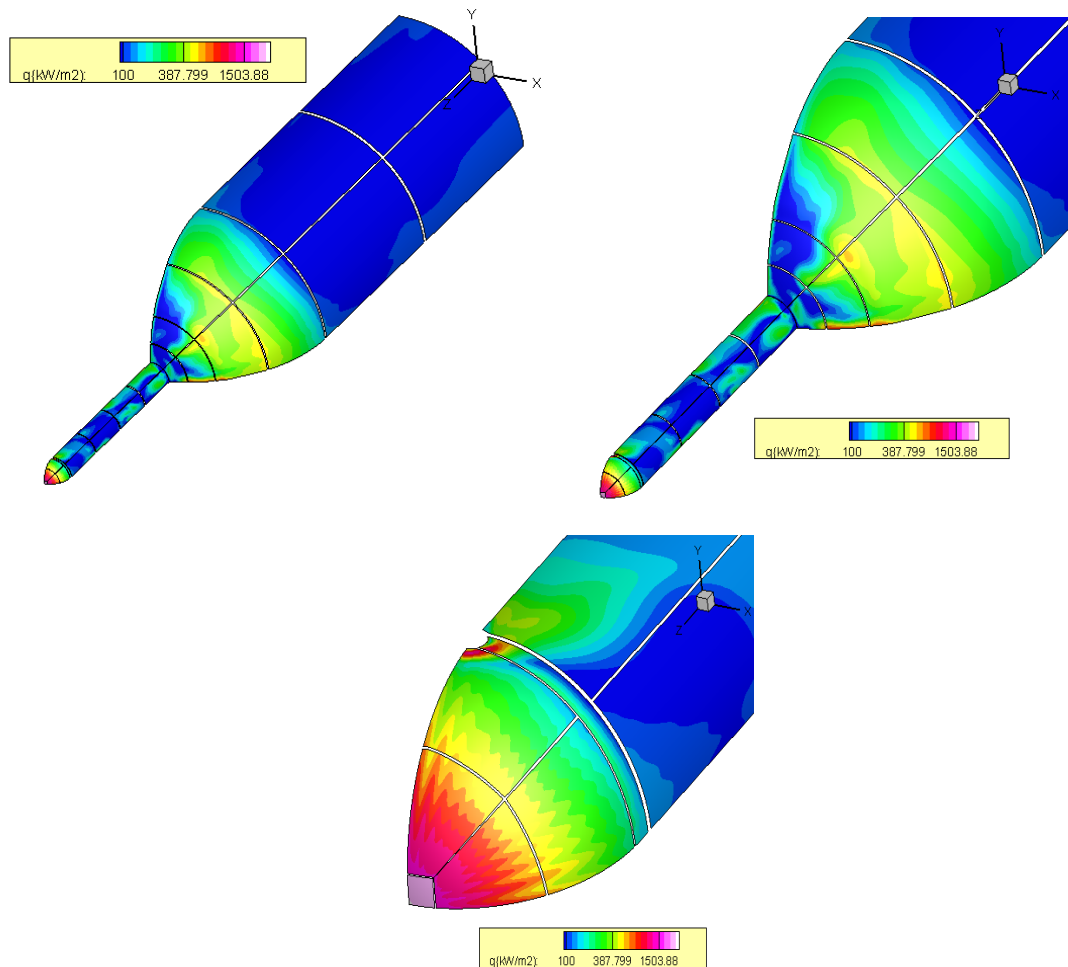

Figure 6.6. Heat flux contours for case A with zoomed view of variation near blunt body(top right) and stagnation region of spike(bottom)

 As expected, the highest amount of heat transfer is in the stagnation region in front of the spike with a heat flux rate of 2520 kW/m^2. The heat flux near the shock-shock interaction point is about 250 kW/m^2 which is lower than the surrounding region by 400 kW/m^2 to 500 kW/m^2. Thus jets contribute to heat flux reduction by creating large recirculation zones. There are spaces in between blocks in the heat transfer plots as the code calculates the values at the cell centers and not at the nodes of the blocks.

6.2 Contour plots for Case B: Laminar with Non-Injection

The contour plots for pressure, v-component of velocity, w-component of velocity, temperature and heat flux for no-jet case are shown below. The peak pressure at the shock-shock interaction point is approximately 39800 Pa. The plots for v-component of velocity in Fig 6.8 are shown here to display the jet injection planes that are set to the no-slip wall condition.
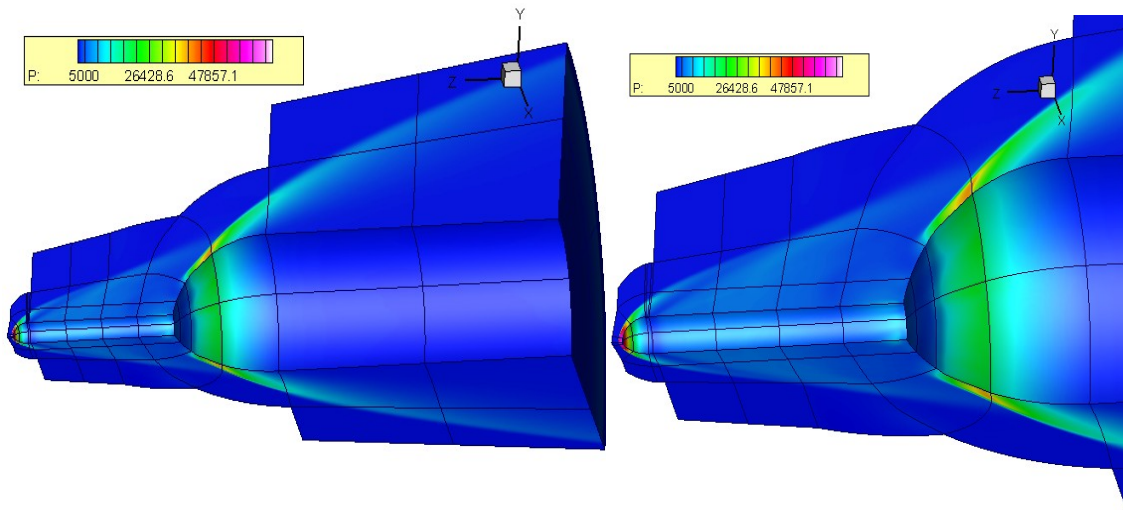

Figure 6.7. Pressure contours for the case B with zoomed view(right)
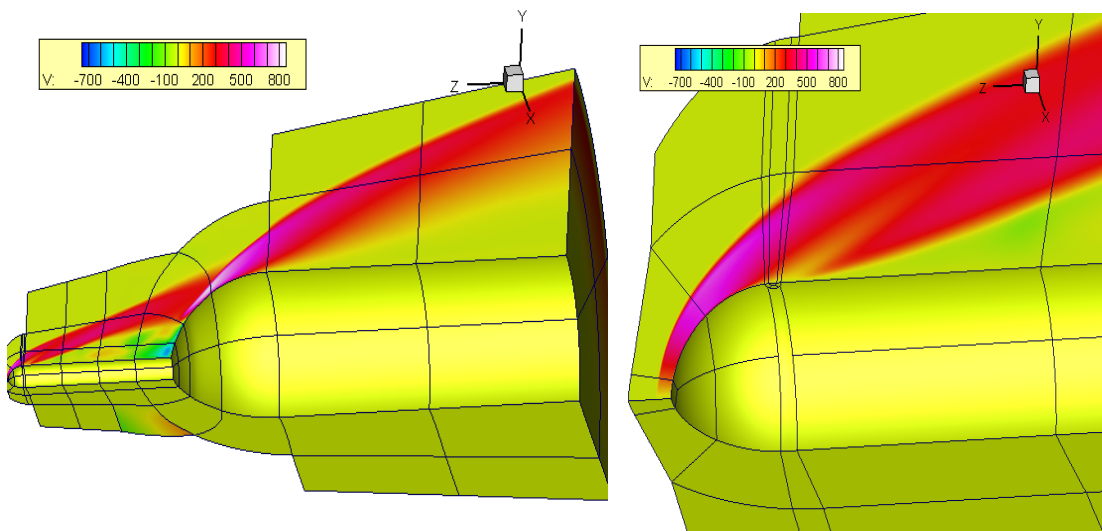

Figure 6.8. Contours for v-component of velocity for case B with zoomed view(right)

As visualized in Fig 6.9, the recirculation zones are smaller when compared to case A. The stagnation temperature is around 1770K. The high temperature zones occur near the nose of the blunt body increasing the chances of ablation. The highest temperature in the region is around 1700K. The heat flux near the flow reattachment point is around 525kW/m^2. The heat flux variation can be seen in Fig 6.11.
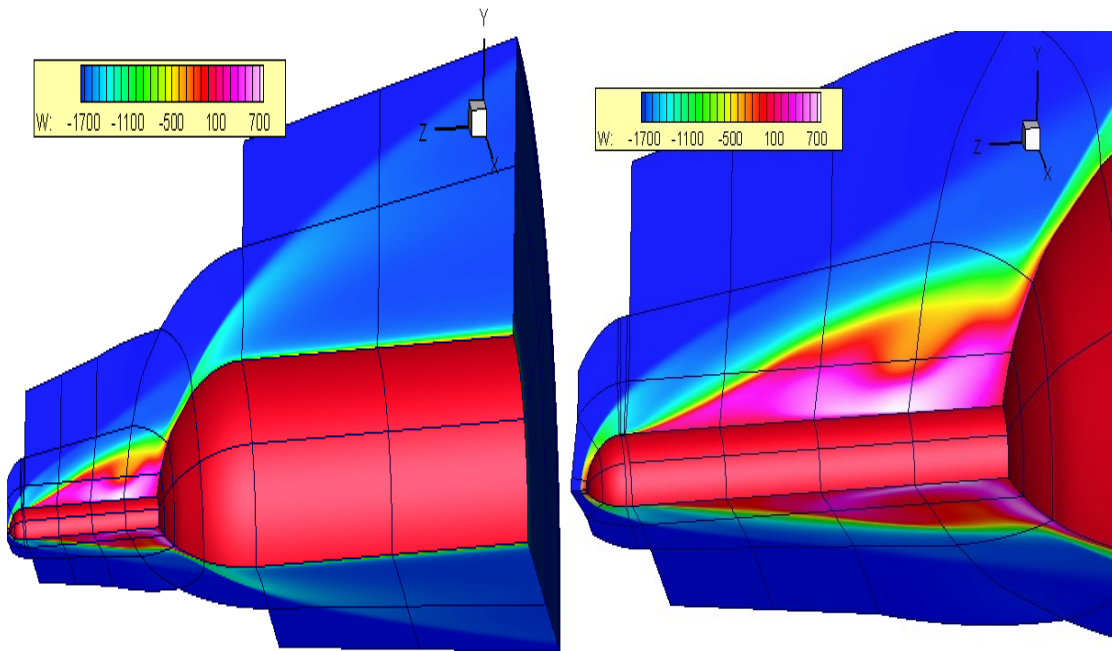

Figure 6.9. Contours for w-component of velocity for case B with zoomed view of recirculation zone(right)
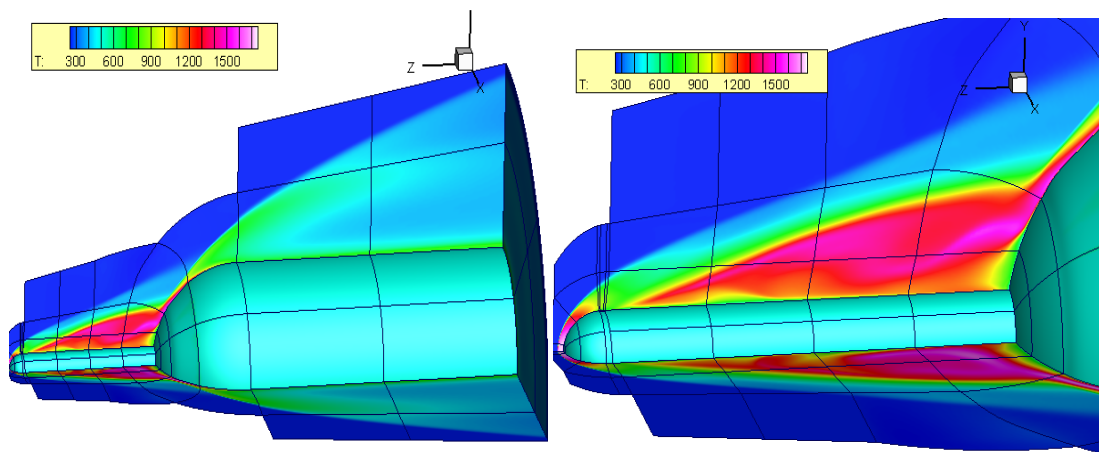

Figure 6.10. Temperature contours for case B with zoomed view of high temperature region on the blunt body(right)
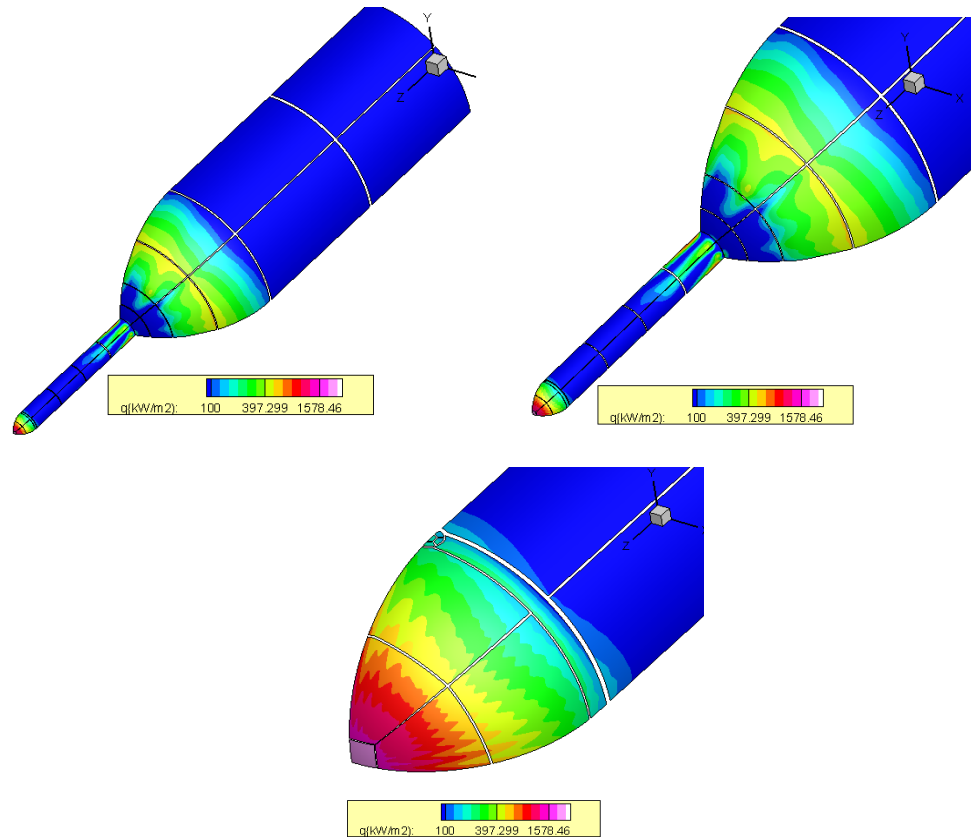
Figure 6.11. Heat flux contours for case B with zoomed view of variation near blunt body(top right) and stagnation region of spike(bottom)

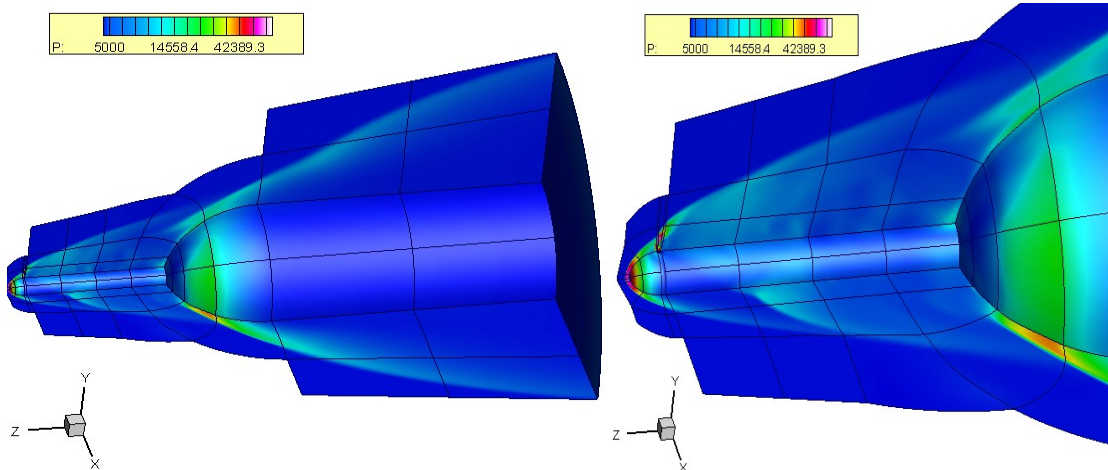## 6.3 Contour plots for Case C: Turbulence with Lateral jet injection

Figure 6.12. Pressure contours for the case C near the blunt body(left) and near the orifice(right)
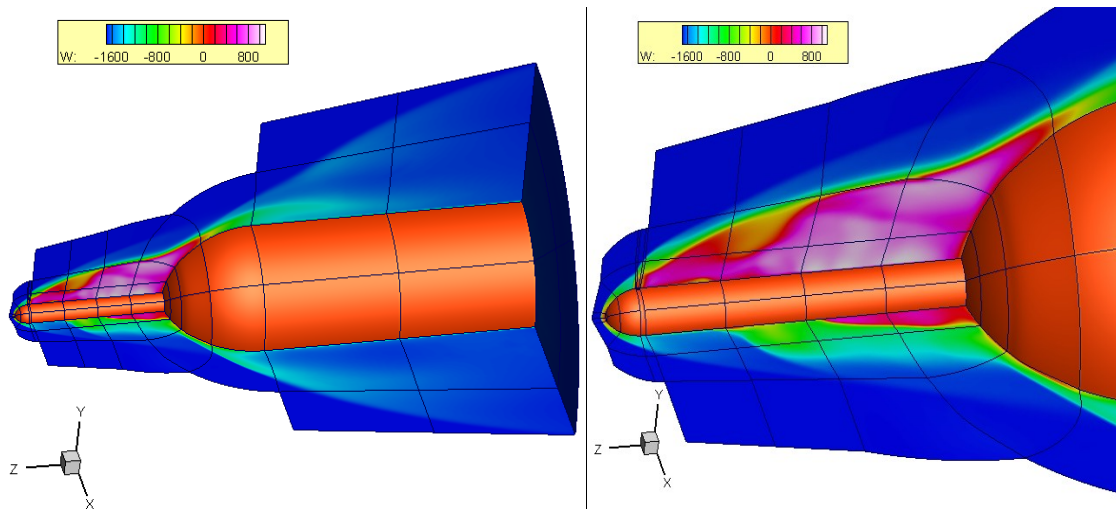
Figure 6.13. Contours for w-component of velocity for case C with zoomed view of recirculation zone(right)

The peak pressure at the flow reattachment point under the influence of the jet is approximately 20350Pa and on the other symmetry plane is around 40400Pa. The reattachment point is pushed rearward as in the laminar case. A rough approximation of the size of the recirculation zone can be made with the help of coordinates. It is observed that it extends up to 64mm in length and 19mm in height for both laminar and turbulent jet injection cases.
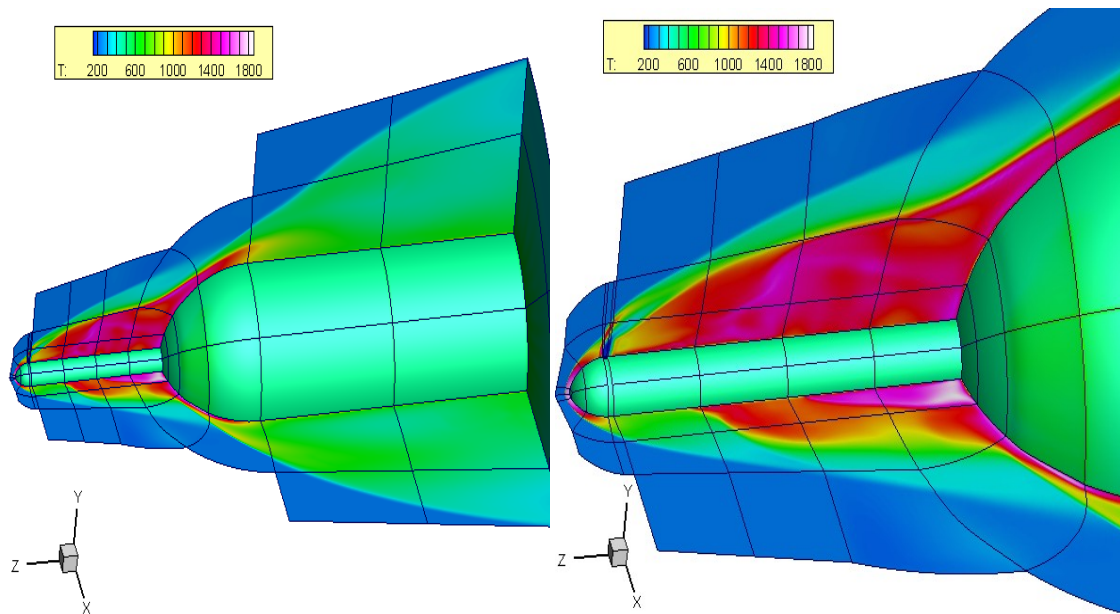

Figure 6.14. Temperature contours for case C with zoomed view of high temperature region on the blunt body(right)
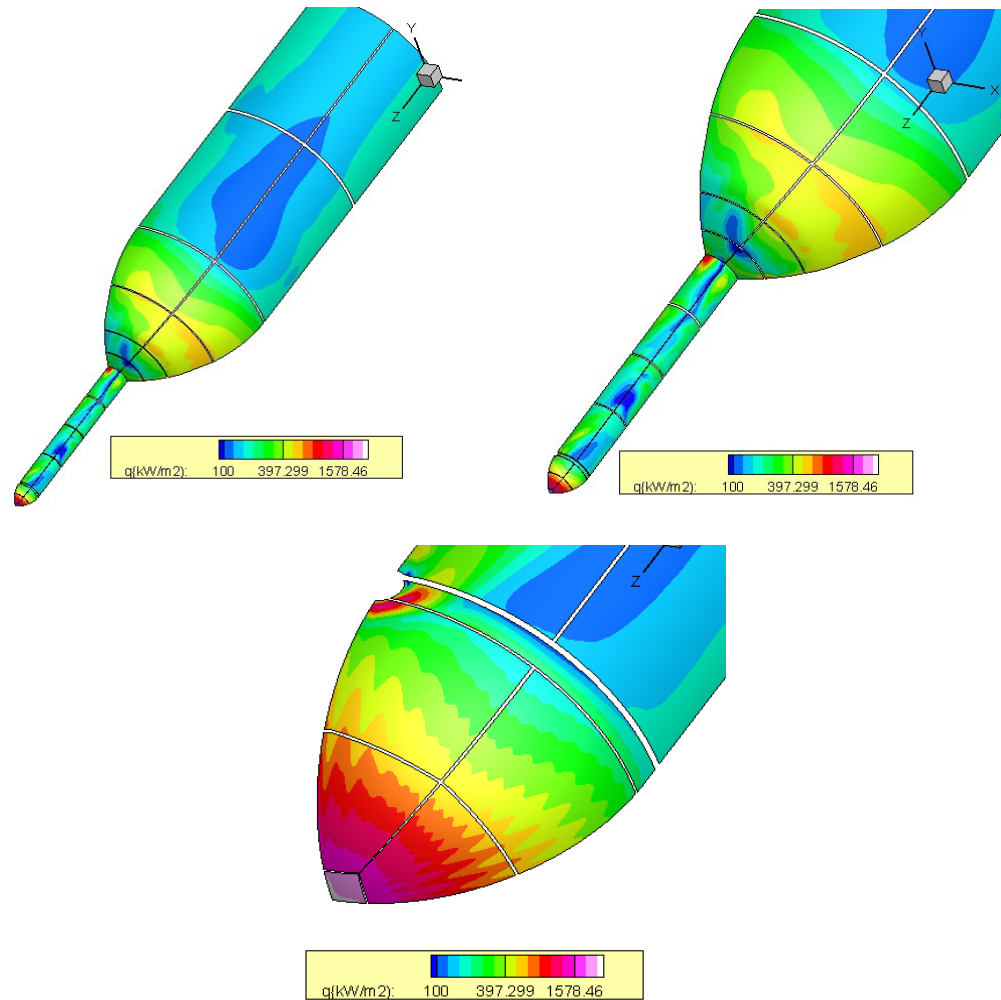
Figure 6.15. Heat flux contours for case C with zoomed view of variation near blunt body(top right) and stagnation region of spike(bottom)

The jet pushes the flow reattachment point rearward. The temperature in its vicinity is 1500K whereas, in the other symmetry plane it is about 1740K which is visible as green patch on the blunt body in Fig 6.14. The heat flux at the stagnation region of the spike is 2570 kW/m^2 which is higher than in case A as expected. Near the recirculation zones it has a value of 275kW/m^2 which increases up to 520 kW/m^2 in the adjacent blocks. The jet is more effective in reducing heat transfer in case A than in case C. For case A the heat flux values vary from 210kW/m^2 to 260kW/m^2 but due to the turbulence the heat flux values vary from 275kW/m^2 to 355kW/m^2.

6.4 Contour plots for Case D: Turbulence with Non-injection
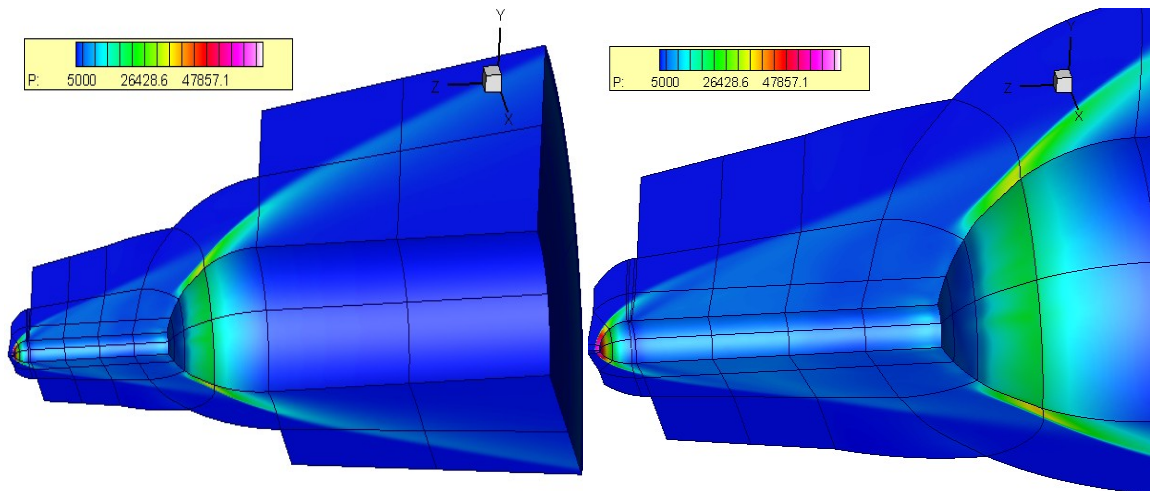
Figure 6.16. Pressure contours for the case D with zoomed view(right)
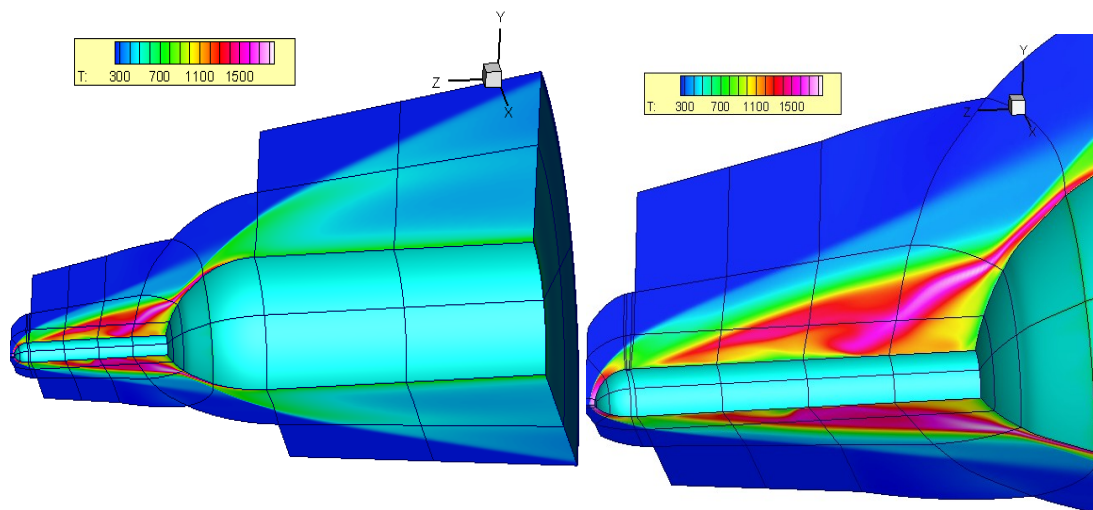
Figure 6.17. Temperature contours for case D with zoomed view of high temperature region on the blunt body(right)

The peak pressure on the blunt body has a value of 37000Pa. The highest temperature encountered at the flow reattachment point on the body is 1740K. The heat flux is the highest in the stagnation region in front of the spike with a value of $2500kW/m^2$ and on the shoulder of the blunt body it is about $560kW/m^2$.
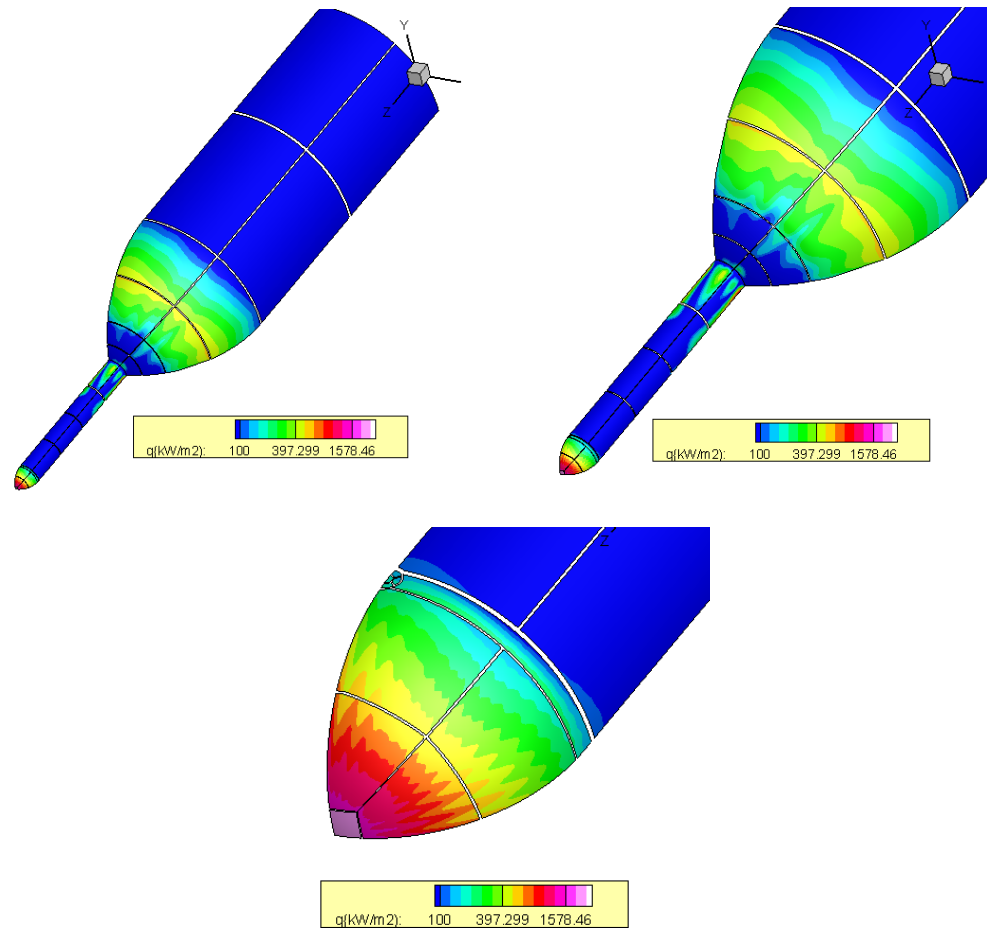
Figure 6.18. Heat flux contours for case D with zoomed view of variation near blunt body(top right) and stagnation region of spike(bottom)

6.5   Comparison of test cases

The heat flux profiles and pressure profiles for different test cases are used to compare and verify the efficiency of the jet in reducing heat transfer and peak pressure at the flow reattachment point on the blunt body.

6.5.1   Pressure Profiles

The geometry is modeled in the z-direction with -0.112m representing the inflow in front of the aero-spike and 0.129m representing the outflow at the end of the domain. In Fig 6.19, it is observed that the largest value of pressure for all the cases occur at

-0.012m, which is the location of stagnation point on the spike. All four cases have the same stagnation pressure of 62000Pa. Using k-ω turbulence model will not affect the results in the stagnation region because the model reduces to a laminar case in its vicinity. The second peak located at z= -0.1 m depicts jet ejection pressure of 47383.55 Pa for cases A and C. The green line for the turbulent with jet case overlaps the blue line for the laminar with jet case, hence it is not visible. The pressure peaks within the region -0.05m < z < 0m are caused by the pressure rise at the flow reattachment points on the blunt body. It can also be seen that the peak pressure at the flow reattachment point is lower for the turbulent case when compared to the laminar case, thus proving to be more effective due to the large boundary layers. It can be inferred from the plots that the peak pressure rise can be reduced by 30.3% for turbulent case and 35.9% for the laminar case.
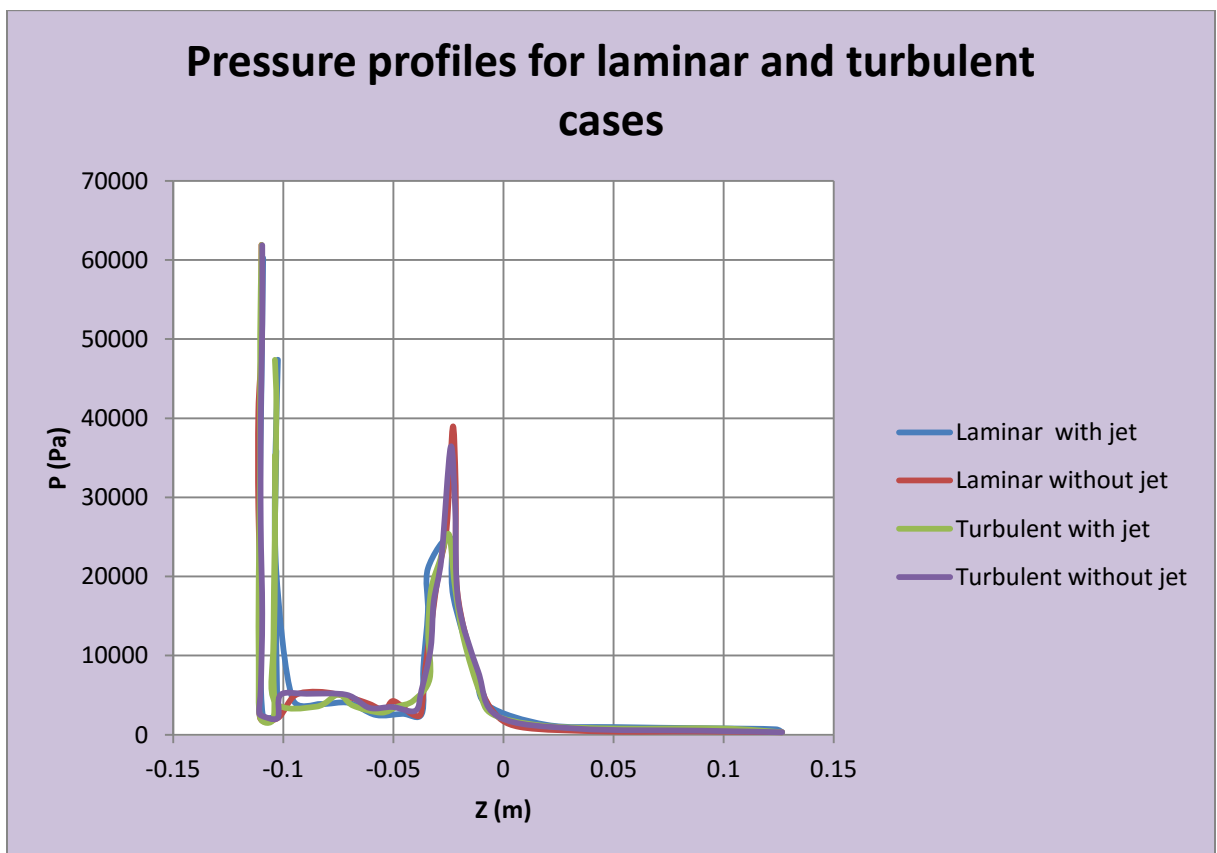

Figure 6.19. Pressure plot for laminar and turbulent cases.

Fig 6.20 shows the comparison of the pressure profiles with the numerical results obtained by Liu and Jiang(2013). The authors didn't provide any details about the grid,

hence a grid comparison is not done here. The Spalart Allmaras model was used to numerically model turbulence and second order schemes were used to solve governing equations in their case. The HYP code used here for research is first order in space with k-ω model used for turbulence modeling. The stagnation points in front of the spike are offset by 0.01m. It is surmised that this is because of the difference in grid generation. The lower order method might damp out transients, hence, a steady state solution was obtained. This might be the result of such large difference in the peak pressures at the shock-shock interaction points near the recirculation region. According to Liu and Jiang (2013), the peak pressure at the reattachment region is reduced by 65% but here the peak pressure reduction of only 30.3% was attained. When compared to the journal article, the x-scale is offset by 0.01m due to the difference in geometry modeling and the x-max (or z-max) is only 0.129m, as only 60% of the blunt body length is modeled.
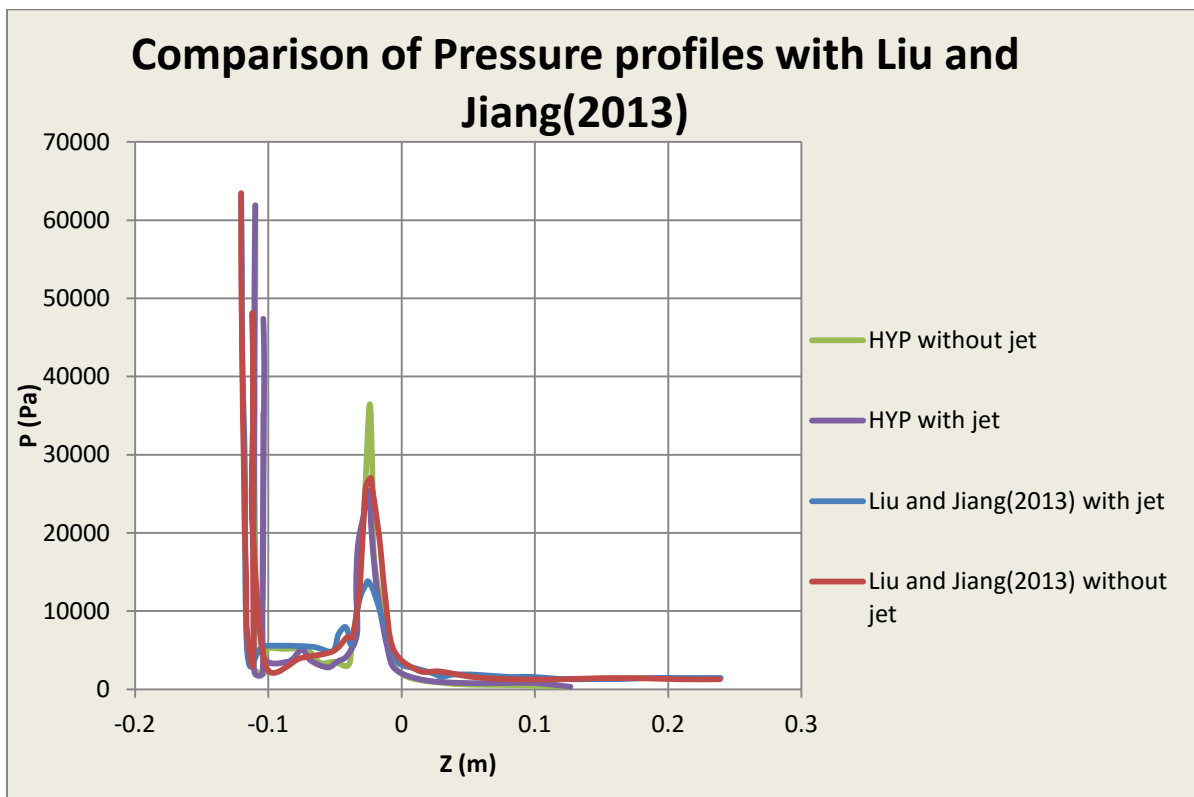

Figure 6.20. Pressure profile comparison with Liu and Jiang (2013).

6.5.2   Heat Flux Profiles

The heat flux profiles for the laminar and the turbulent cases are shown in Fig 6.21. The heat transfer is maximum in the stagnation region of the spike for both the cases with and without jet injection. The flow reattachment zone extends from z value of -0.06m to -0.03m. It is observed the heat flux value for jet injection case is around 310 kW/m^2 and that for the non-injection case is around 870 kW/m^2. This produces a heat flux reduction of 54.1% for the laminar case and 64.3% for the turbulent case.
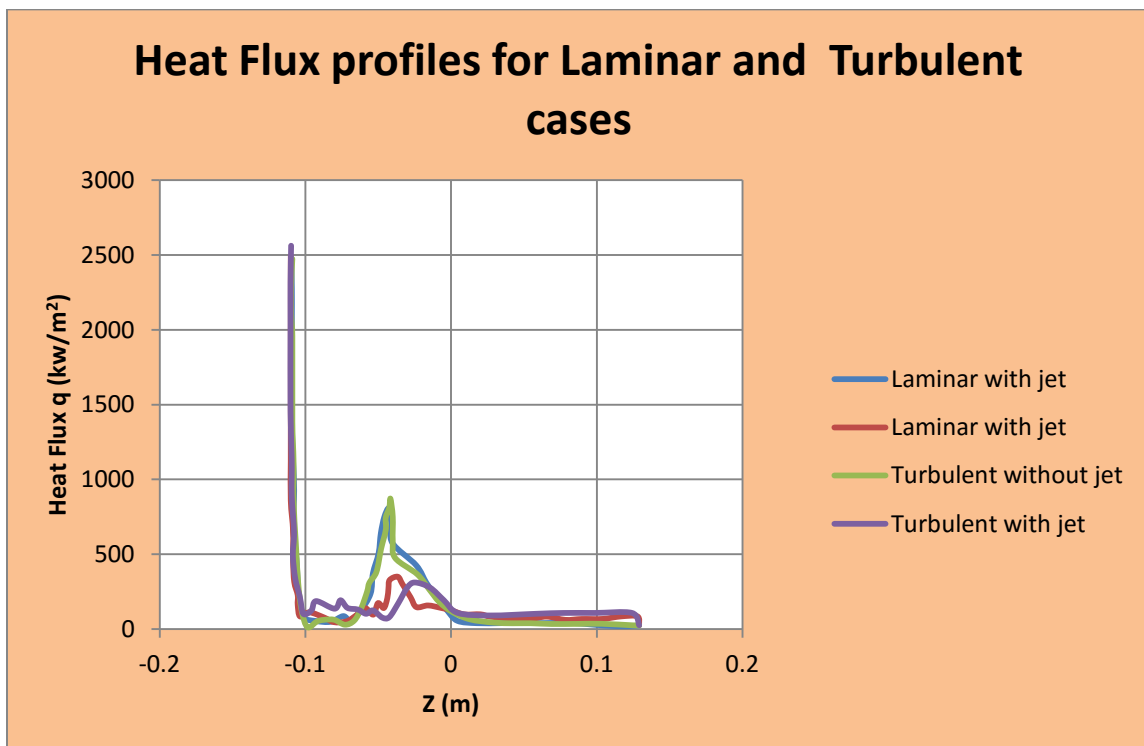
Figure 6.21. Heat flux plot for laminar and turbulent cases

According to Liu and Jiang (2013), a heat flux reduction of 56% can be obtained at zero degree angle of attack. Fig 6.22 provides a comparison of the results with the journal article by Liu and Jiang(2013). As mentioned earlier, dampening the transients might explain the high heat flux values obtained by HYP thus resulting in a higher heat flux reduction of 64.3%. The profiles also show a higher stagnation heat transfer with the

location of stagnation point offset by 0.035m when compared to Liu and Jiang(2013). This offset cannot be accounted for without proper grid information from the authors.
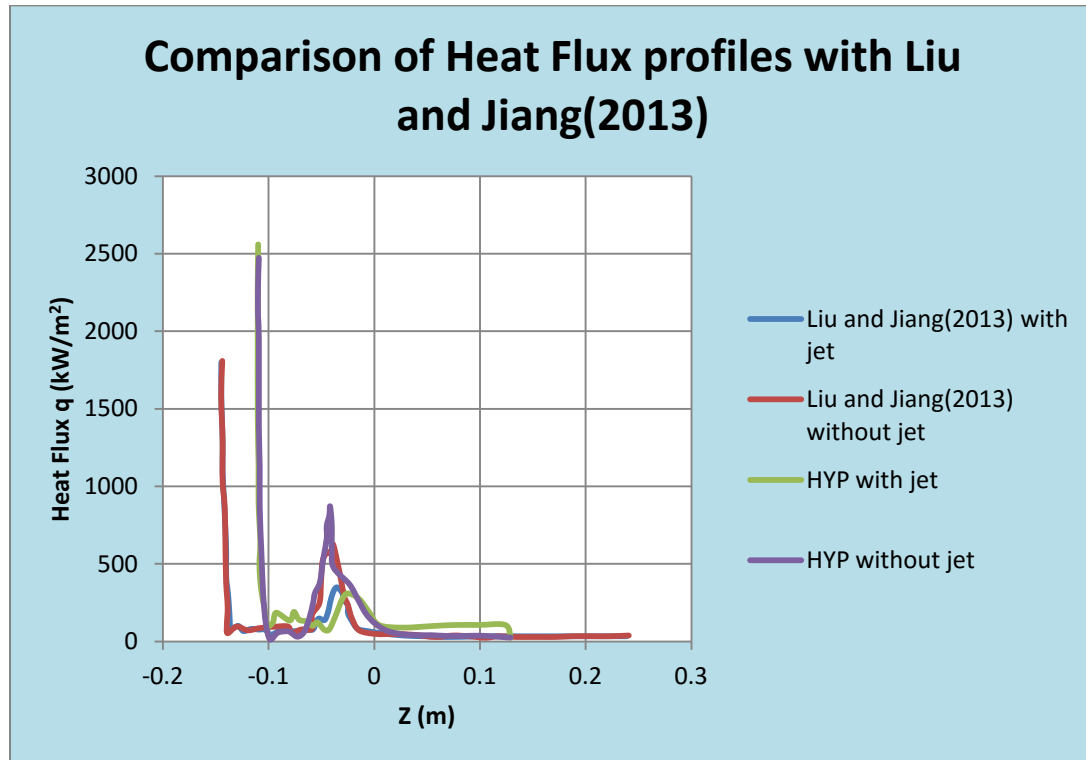
Figure 6.22. Heat Flux profile obtained by Liu and Jiang(2013).

6.6   Drag Calculation

The drag calculation is described in a separate sub-section because this cannot be compared with Liu and Jiang (2013). The journal article does not describe the method used for calculating drag for the test cases. According to Liu and Jiang (2013), "The shock wave drag inferred from the pressure measurements is reduced by 33 %"(p. 589). The pressure measurements in Liu and Jiang(2013) were taken on the windward side only along the shoulder of the blunt body and the drag reduction was calculated according to pressure reductions. When the authors were contacted, they stated that their research was mainly focused on calculating the peak pressure and heat flux reduction at the flow reattachment points instead of drag reduction["Personal Communication with Liu and Jiang(2013)].

In this report, the drag is calculated by integrating the change in the pressure and the momentum fluxes across the control volume in the z-direction. The inflow plane is selected upstream of the computational domain where values of w-component of velocity and the pressure remain constant. The four outflow domains are considered as an outflow plane.

Applying Newton's second law for the above case, the drag on the fluid is given by,

$$D_{fluid} = \left(\rho w^2 A\big|_{out} - \rho w^2 A\big|_{in}\right) + \left(PA\big|_{out} - PA\big|_{in}\right) \tag{7.1}$$

$$D_{body} = -D_{fluid} \tag{7.2}$$

The integrated value of pressure flux and the momentum flux for the three outflow domains is calculated by the code. Using them, the drag for each test cases is calculated manually. The drag values on the body for each case are displayed in Table 6.1. These values have to be multiplied by four to obtain the value of drag on the whole body as quarter symmetry was considered. The article published by Liu and Jiang(2013) does not provide any drag values which can be used for comparison.

Table 6.1. Drag values for 4 test cases

Test Case	Drag (N)
Case A: Laminar with Lateral jet injection	65.6
Case B: Laminar with Non-Injection	22.5
Case C: Turbulence with Lateral jet injection	66.8
Case D: Turbulence with Non-injection	27.3

Analyzing the results, it is found that the drag increases by 65.7% for the laminar case and by 59.1% for the turbulent case. This contradicts the proposition of the journal article. This may be because the effect of base drag is not considered during the drag calculations as the flow conditions near the base are unknown.

7. Conclusion

The aim of this thesis has been to investigate a new concept of Non-Ablative Thermal Protection System proposed by Liu and Jiang(2013) which utilizes a spike-lateral jet combination to mitigate the heat transfer and drag in hypersonic vehicles. According to the concept proposed, the lateral jet injection pushes the shock away and creates a larger recirculation region which reduces drag and heat transfer on the body.

Numerical studies are conducted on a hemispherical spike attached to a blunt nose cone at freestream Mach number of 6 and zero degree angle of attack. The grid spacing is calculated by determining the Reynolds number of the flow and the y+ values. Four cases are tested: with and without lateral jet injection each for a laminar and a turbulent flow case. The results show that lateral jet injection can reduce the peak pressure at the flow reattachment point on the blunt body by 35.9% and 30.3% for the laminar and turbulent cases respectively. Nevertheless, the results are not comparable with the 65% reduction in peak pressure obtained by Liu and Jiang (2013). A reduction in heat flux of 54.1% for laminar case and 64.3% for the turbulent case is obtained compared with the 56% heat reduction proposed by the journal article.

Drag calculations are based on change in momentum flux and pressure across the control volume. From the drag calculations, the lateral jet injection increases drag by 65.7% and 59.1% for laminar and turbulent cases respectively. The base drag is neglected in the above calculations due to insufficient data.

Analyses of the results show that the spike-lateral jet injection method can be used as an effective method for reducing peak pressure and heat flux at the shock-shock interaction points on the nose cones but it may be ineffective in reducing drag. The jet injection through the two orifices modifies a very small region of the flow field in front of the blunt body. The remaining portion of the body being subjected to a high pressure and temperature becomes susceptible to ablation. Other new methods have to be proposed to overcome the drawbacks of the current techniques.

REFERENCES

Anderson, J.D., Jr. (1995). Computational Fluid Dynamics: The Basics with Application
        New York: McGraw-Hill.

Aruna, S. and Anjalidevi, S.P. (2013). A computational study on effect of Forward
        Facing Jet toward mitigation of drag on a Tangent ogive body in Hypersonic
        Turbulent flow. International Journal of Applied Mathematics and Mechanics,
        Vol. 9, No. 2, pp. 80-94.

Dolling, D.S. and Murphy, M.T.(1983). Unsteadiness of the separation Shock Wave
        Structure in a Supersonic Compression Ramp Flowfield. AIAA, Vol. 21, No.12,
        pp. 1628-1634.

Gauer, M. and Paull, A. (2008). Numerical investigation of Spiked Blunt Nose Cone at
        Hypersonic speeds. Journal of Spacecrafts and Rockets, Vol. 45, No. 3.

Hirsh, C. (1990). Numerical Computation of Internal and External Flows. Vol. 2.
        New York: Wiley.

Holman, J.P. (2010). Heat Transfer. (Tenth ed.). Boston: McGraw-Hill.

Horvath, Martin. (2010). Extension of multiple species of a Two-Equation Turbulence
        Model for high speed flows. Unpublished master's thesis, Embry-Riddle
        Aeronautical University, Daytona Beach, United States.

Liu, Yenfeng and Jiang, Zonglin. (2013). Concept of Non-Ablative Thermal Protection
        System for Hypersonic Vehicles. AIAA, Vol. 51, No. 3.

Mehta, R.C. (2000). Numerical heat transfer study over spiked blunt bodies at Mach 6.8.
        Journal of Spacecrafts and Rockets, Vol. 37, No. 5, pp. 700-703.

Meyer, Benjamin., Nelson, H. F and Riggins, David W. (2001). Hypersonic Drag and
        Heat transfer reduction using a Forward-Facing Jet. Journal of Aircraft, Vol. 38,
        No.4.

Motoyama, Noboru., Mihara, Ken., Miyajima, Ryo., Watanuki, Tadaharu and Kubota,
        Hirotoshi. (2001). Thermal Protection and Drag Reduction with use of spike in
        Hypersonic flow. AIAA/NAL-NASDA-ISAS, 10th International Space Planes
        and Hypersonic Systems and Technologies Conference.

Remeo, D.J. and Sterrett J.R. (1963). Exploratory Investigation of the effect of Forward-
        Facing Jet on the Bow Shock of a blunt body in a Mach Number 6 Free Stream.
        NASA TN D-1605.

Schlichting, H. and Gersten, K. (2000). Boundary Layer Theory. (Eighth ed.). New York: Springer.

Schmitt, F. and Perrell, E. (2006). The HYP CFD User's Manual. Ver. 1.0. Unpublished Manual.

Settles, G.S., Vas, I.E., and Bogdonoff, S.M. (1976). Details of a Shock Separated Turbulent Boundary Layer at a Compression Corner. AIAA, Vol. 14, No. 12, pp. 1709-1715.

Steger, J.L. and Warming, R.F. (1979). Flux Vector Splitting of the Inviscid Gasdynamic Equations with Application to Finite-Difference Methods. NASA TM-78605.

Tannehill, J.C., Anderson, D.A. and Pletcher, R.H. (2013). (Third ed.). New York: Taylor And Francis.

Wilcox, D.C. (1993). Comparison of Two-Equation turbulence models for Boundary Layers with Pressure Gradient. AIAA, Vol. 31, No. 8, pp. 1414-1421.

Wilcox, D.C. (2006). Turbulence Modeling for CFD. (Third ed.). DCW Industries, Inc.